Mechanical performance of prefabricated concrete beam-column joints with double-grouted sleeve connectors: A numerical and theoretical study

Zhiwei Lu [a,b], Bin Wu [a,c,*], Hiroyasu Sakata [b], Jun Huang [d], Mingzhong Zhang [e]

[a] *School of Civil Engineering and Architecture, Wuhan University of Technology, Wuhan, 430070, China*

[b] *Department of Architecture and Building Engineering, Tokyo Institute of Technology, Tokyo, 152-8550, Japan*

[c] *Sanya Science and Education Innovation Park of Wuhan University of Technology, Sanya, 572000, China*

[d] *Hubei Industrial Construction Group Co., Ltd., Wuhan, China*

[e] *Department of Civil, Environmental and Geomatic Engineering, University College London, London, WC1E 6BT, UK*

Abstract: This paper presents a systematic numerical study on the structural performance of a newly developed quick-buildable beam-column joint with double-grouted sleeves considering its surface-to-surface contact behaviour between the prefabricated concrete and grouting mortar and strain penetration of the transition rebar. Theoretical analysis is also conducted to predict the load-bearing capacity of the proposed connection. After validation with experimental data, the finite element model is employed to investigate the effects of different factors including protruding beam length and grouting mortar thickness on the structural behaviour of the joint. Results indicate that the maximum stress of the reinforcing bars in the joint with no protruding beam is approximately 15.0% greater than that with a protruding beam, while the maximum stress of the joint anchorage bars decreases by around 87.0% when the short sleeves are placed completely in the joint core area. As the protruding beam length increases, the maximum crack width drops rapidly first and then slowly with a turning point of 1.36 times the short sleeve length, and the highest load-bearing capacity is achieved when the protruding beam length and short sleeve length equal. With the rising grouting mortar thickness, the maximum stress of the transition rebar reduces rapidly first and then slowly with an inflexion point of 50 mm. The change in eccentricity of the transition rebar leads to an around 3% change in the load-bearing capacity of the joint without a projecting beam. The theoretical predictions are in

* Corresponding author. E-mail address: wub@whut.edu.cn (B. Wu).

satisfactory agreement with numerical results and can be adopted for practical engineering design.

Keywords: Finite element analysis; Prefabricated concrete joints; Double-grouted sleeves; Protruding beam; Rapid construction; Parametric analysis

1. Introduction

Prefabricated reinforced concrete structures are gradually accepted as an alternative to some conventional monolithic reinforced concrete structures for different practical applications because of less environmental impact, good quality, reduction in formwork, and accelerated construction speed [1-4]. To upgrade the construction industry, the Chinese government announced that the application ratio of precast structures including prefabricated concrete, steel, and wood structures ought to be over 30% in new construction through approximately ten years of effort [5]. The ratio should reach 40 to 55% in some provinces and municipalities by 2025 [6-8]. The damage and failure of prefabricated reinforced concrete buildings subjected to earthquakes often result from poorly designed connection systems. Therefore, their seismic response including stiffness, strength, deformability, and ductility is highly dependent on the mechanical performance of the links between prefabricated members [9-14].

For prefabricated concrete frame structures, the connections between prefabricated beams and columns play a critical role and thus reasonable design of the beam-column joints is of great importance. In recent years, various beam-column joints have been proposed to tackle the linking problems in prefabricated concrete frame buildings such as dowel pin connections [15-18], welded connections [19-23], bolted connections [24-29], prestressed connections [30-35], rebar lapping splice connections [36-40], and mechanical sleeve and spiral-confined splice connections [41-45]. Although dowel pin connections with controllable tolerances are easy to fabricate, they are only commonly used in single-story industrial and low-rise residential buildings due to relatively lower stiffness and distinctive force transmission mechanism. Welded connections have high dependence on the welding quality, and the installation costs may rise as the welding construction needs to be carried out by experienced and skilled workers [20]. The seismic performance of the beam-column joints with bolted connections can be significantly improved by introducing energy dissipation devices. However, bolted joints may cause additional steel consumption problems and require very compact tolerances for the precast members, which may still be a great challenge for some manufactures of prefabricated units [46]. The prefabricated frame structures with prestressed

connections have the advantages of minor damage and lower residual deformation of structural elements under earthquakes. However, this type of connection with lower energy dissipation capacity resulting from the lower inherent damping due to the post-tension method frequently requires the installation of energy dissipation devices to enhance its seismic capacity [47]. Since rebar lapping splice connections can be designed to make their structural behaviour emulative to the monolithic connections, they have been widely used. Nevertheless, the rebar lapping method used in the core zone of beam-column joints frequently results in reinforcement congestion problems and construction defects in the connection zone of the joint with rebar tying and in-situ concrete pouring. To tackle these shortcomings, another kind of emulative connection, i.e., mechanical sleeve and spiral-confined splice connections, was developed to move the connection region to the beam end outside the core area of the beam-column joint. For instance, Yan et al. [41] proposed and tested a type of precast beam-column joint with single-grouted sleeves and found that the seismic response of the proposed connection was similar to that of the reference counterpart and grouted sleeves affected the performance of beam's plastic hinge. Ma et al. [45] explored a beam-column joint connected using grouted spiral-confined lap splices under reverse lateral loading and reported that the developed linking approach can be used in seismic zones owing to its superior seismic behaviour compared with monolithic joint. However, the existing mechanical coupler and spiral-confined splice connections still require rebar tying and post-concrete pouring on site.

To solve the above-mentioned limitations, the authors recently proposed a novel prefabricated beam-column connection linked using double-grouted sleeve connectors, as shown in Fig. 1 [48]. Such connection has the prominent advantages of shorter linking length (only around 30 mm), larger controllable tolerances provided by the short and long sleeves with a larger inner diameter, and eliminating the projecting steel bars from the prefabricated components which may cause injury. Besides, on-site concrete casting and tying of reinforcement are also eliminated, which can significantly accelerate construction and save costs.

Note that considering the cost and time consuming, only a small number of precast specimens connected using double-grouted sleeves were experimentally investigated in Ref. [48]. A systematic numerical study is therefore required to complement the experimental work to explore the effects of different factors on the mechanical performance of the proposed joint. Macro-level joint models and continuum-based finite element models are usually employed for prefabricated beam-column joints

[49]. The macro-level joint models are mainly applied to analyse the entire or part of the frame structures and cannot be effectively utilised to simulate the mechanical performance of a joint or connection segment, while a three-dimensional (3D) continuum-based finite element (FE) model is more elaborate and can reflect the detailed response in the crucial region of the joint. It was reported that it is challenging to simulate the pinching effects of load-displacement response under cyclic loading with large deflections [50-52], while the simulated monotonic load-displacement curves that represent an envelope of hysteretic response using finite element method was found to agree well with the experimental data [25, 53-55].

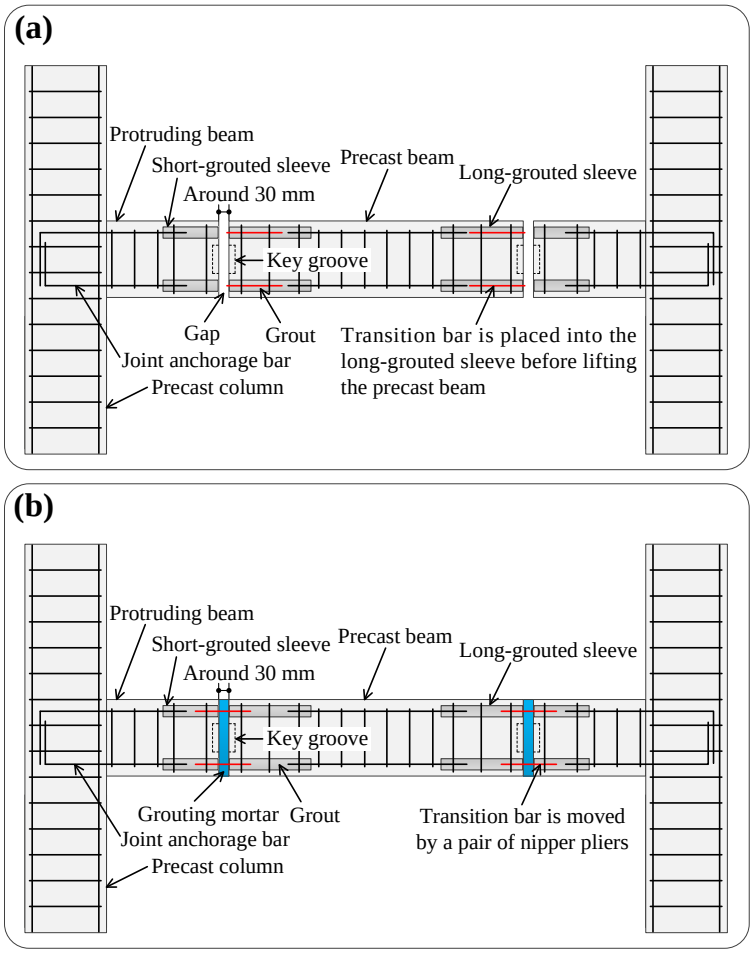

Fig. 1. Schematic diagram of the developed prefabricated frame structure linked using double-grouted sleeve connectors: (a) precast column and beam in place; (b) after installation.

The primary purpose of this study is to systematically investigate the structural behaviour of the newly proposed fast-installable beam-column joint linked by double-grouted sleeve connectors under monotonic loading using FE method implemented with Abaqus^{①} software. The surface-to-surface contact between the grouting mortar and prefabricated concrete and the strain penetration of the transition rebar in the double-grouted sleeve splice are taken into consideration in FE model which is validated with the corresponding experimental results presented in a previous study [48] in terms of

load-deflection response and failure modes. Afterwards, a series of simulations are conducted using the validated FE model to estimate the stress distribution of the steel cages and sleeves as well as the effects of some critical parameters including the protruding beam length, grouting mortar thickness, strengths of grouting mortar and precast concrete, and rebar diameter and eccentricity on the structural performance of the developed joint with double-grouted sleeves. Finally, theoretical analysis is undertaken to predict the load-carrying capacity of the proposed joint with various diameters of rebar considering the determination of failure control cross-section, the predictions of which are compared with numerical results to gain insights into the underlying mechanisms.

2. Finite element modelling

2.1 Model configuration

In this study, three prefabricated beam-column joints with no protruding beam (BCJ-1 to BCJ-3), two precast beam-column joints with a protruding beam of 425 mm (BCJ-4 and BCJ-5), and one cast-in-place beam-column joint (BCJ-C) tested in a previous study [48] are selected and modelled using Abaqus to predict the structural behaviour of the prefabricated beam-column joint with double-grouted sleeve connectors in comparison with that of cast-in-place counterpart. For each model, the beam with a total length of 1500 mm has a cross-section of $200\ \text{mm} \times 350\ \text{mm}$ and the column with an entire height of 1500 mm has a cross-section of $350\ \text{mm} \times 350\ \text{mm}$. The dimensions of the key groove on both sides of the gap are $100\ \text{mm} \times 150\ \text{mm} \times 25\ \text{mm}$, and its depth is 5 mm less than that of the designed counterpart to account for the uneven distribution of keyway depths resulting from manufacturing the samples. All columns are reinforced with 8 longitudinal bars with a same diameter of 16 mm and rectangular hoop of 8 mm @ 100 mm. All beams contain 4 longitudinal bars with a same diameter of 16 mm. The rectangular hoop of 8 mm @ 100 mm for all beams is chosen as transverse reinforcement, while its space is less than 100 mm in some local zone for the prefabricated joints. The effects of two lengths of 0 and 425 mm for the protruding beam, 16 and 18 mm for the transition rebars, and grouted sleeve with wedges (GSW) and grouted sleeve with wedges and threads (GSWT) for the grouted sleeves on the structural performance of the joint are considered.

Because rubber sleeves were installed with a hole in the centre of cross-section at the ends of the steel sleeves during the stage of preparing the precast columns and beams [48], the transition bars were approximately located at the centre line of the grouted sleeves. Thus, the centre line of the transition bars can be the same as that of the grouted sleeves when establishing the FE model.

2.2 Element type and mesh size

A half model established symmetrically with regard to the longitudinal axis of the specimens at the centroid of the cross-section is adopted to reduce the computational costs given the symmetry of the joints and loading conditions. The precast concrete, grout, grouting mortar, sleeves, and loading plate are modelled using eight-node linear brick reduced integration hexahedral solid elements (C3D8R). Elements with reduced-integration are selected because they can reduce computer run time [56]. Two-node linear 3D truss elements (T3D2) commonly used in FE analysis are adopted for modelling the reinforcement and transition rebar [26, 49, 52, 55-57]. All mesh sizes for different model members are determined by the mesh sensitive analysis conducted to achieve a satisfactory compromise between computational efficiency and accuracy. Finer and coarse meshes are used in important areas and some other regions, respectively. The FE meshes for the entire beam-column joints are illustrated in Fig. 2.

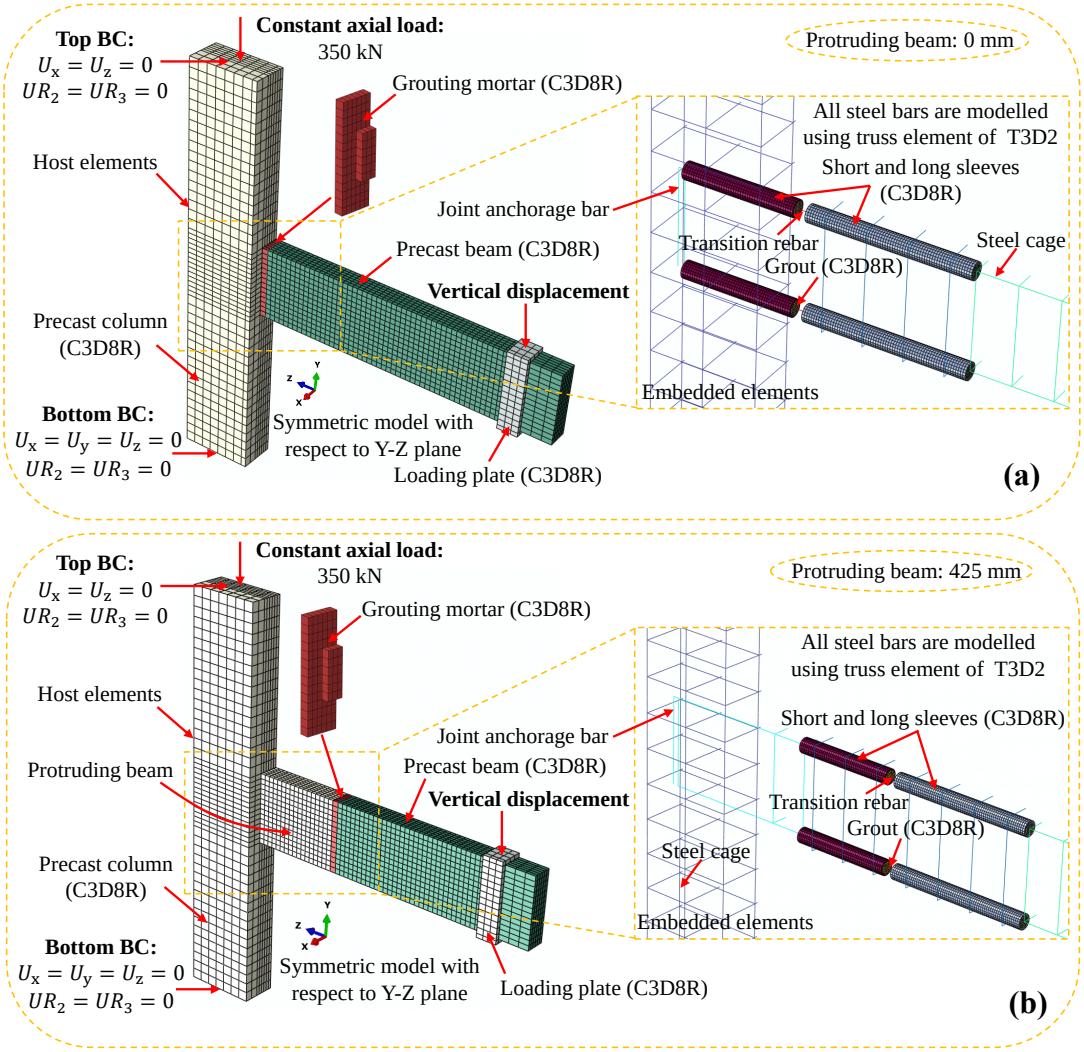

Fig. 2. Finite element models for the prefabricated beam-column joint linked using double-grouted sleeve connectors: (a) with no protruding beam (BCJ-1 to BCJ-3); (b) with a protruding beam of

425 mm (BCJ-4 and BCJ-5).

2.3 Contact properties

The surface-to-surface hard contact is chosen to model the normal behaviour between the precast concrete and grouting mortar with a friction coefficient of 0.67 for tangential behaviour as per Ref. [26] and trial calculations. As no significant bond slip occurs between the grout and sleeve in the experimental tests, the sleeve can be simplified into a common steel pipe and the effects of wedges and threads can be ignored. Hence, the outer surface of the grout is bounded to the inner wall surface of the simplified sleeve by "Tie" constraint. The loading plate is tied on the beam end for avoiding stress concentration and applying vertical loading. The reinforcing bars, transition bars, sleeves, and grout are embedded in the model with an assumption of perfect bond employed.

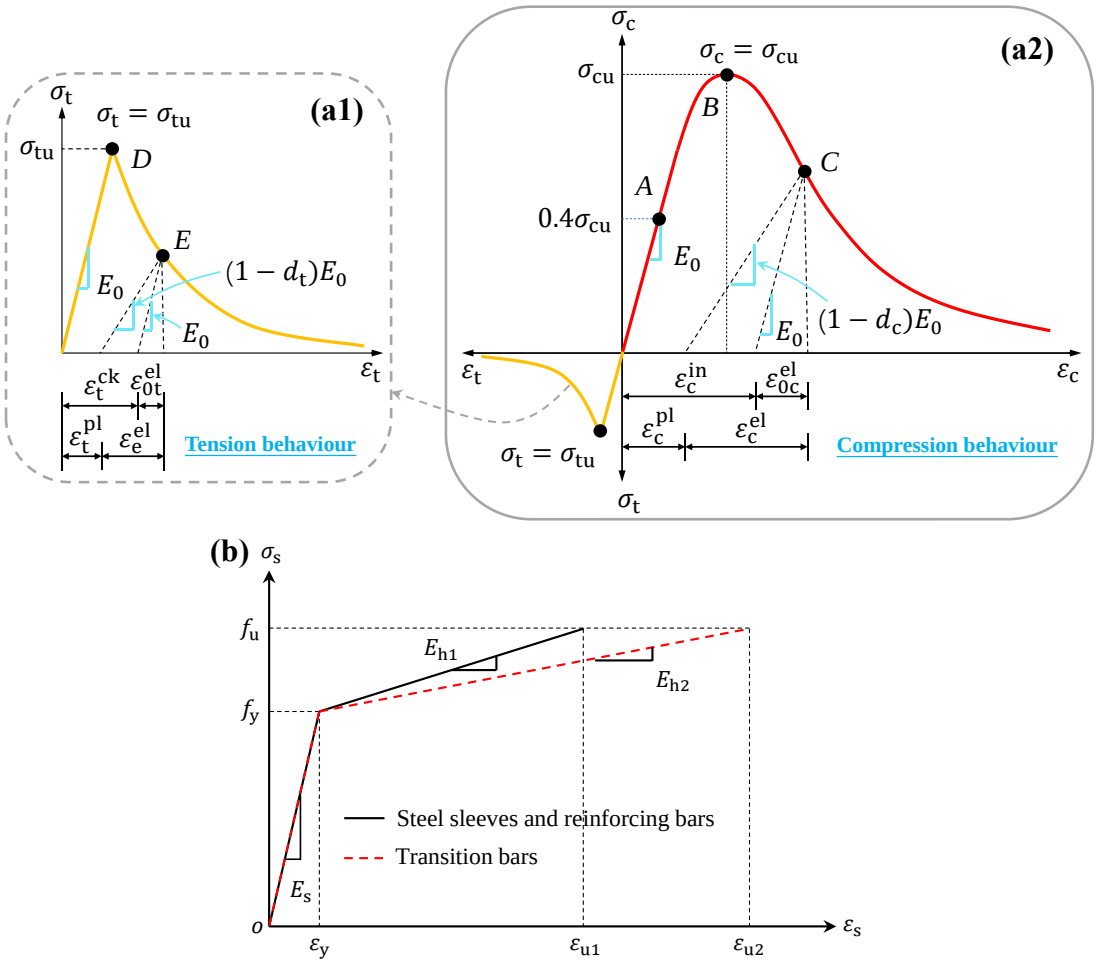

Fig. 3. Stress-strain relationships of: (a) precast concrete, grout, and grouting mortar for CDP model; (b) steel sleeves, reinforcing bars, and transition bars.

2.4 Material models

2.4.1 Concrete, grout, and grouting mortar

The grout and grouting mortar are essentially cement-based materials and there is no specialised constitutive relationship for these materials. Thus, the constitutive models for concrete are applied to

approximately simulate the grout and grouting mortar. In practice, the concrete damage plasticity (CDP) model is employed in Abaqus (Fig. 3a), which is able to predict the elastic-plastic behaviour of concrete for tension and compression damage characteristics. The concrete uniaxial compression and tension stress-strain relationship provided by GB50010-2010 [58] is adopted. The compression stress-strain behaviour can be expressed as follows:

$$\sigma_c = (1 - D_c)E_c\varepsilon_c \tag{1}$$

$$D_c = \begin{cases} 1 - \frac{\rho_c n}{n - 1 + x_c^{\,n}} & x_c \le 1 \\ 1 - \frac{\rho_c}{\alpha_c(x_c - 1)^2 + x_c} & x_c > 1 \end{cases} \tag{2}$$

$$\rho_c = \frac{f_{c,r}}{E_c\varepsilon_{c,r}} \tag{3}$$

$$n = \frac{E_c\varepsilon_{c,r}}{E_c\varepsilon_{c,r} - f_{c,r}} \tag{4}$$

$$x_c = \frac{\varepsilon_c}{\varepsilon_{c,r}} \tag{5}$$

where E_c is the elastic modulus, $f_{c,r}$ is the axial compression strength, α_c is the parameter of descending segment of the curve, and $\varepsilon_{c,r}$ is the strain at the compression peak stress according to [59]. The compression stress increases linearly with an increase in strain before the stress reaches 40% of the peak stress.

It is assumed that the tension stress-strain curve is linear before reaching the maximum stress, but after that, the tension stress-strain response can be described as follows:

$$\sigma_t = (1 - D_t)E_c\varepsilon_t \tag{6}$$

$$D_t = \begin{cases} 1 - \rho_t[1.2 - 0.2x_t^{\,5}] & x_t \le 1 \\ 1 - \frac{\rho_t}{\alpha_t(x_t - 1)^{1.7} + x_t} & x_t > 1 \end{cases} \tag{7}$$

$$x_t = \frac{\varepsilon_t}{\varepsilon_{t,r}} \tag{8}$$

$$\rho_t = \frac{f_{t,r}}{E_c\varepsilon_{t,r}} \tag{9}$$

$$\varepsilon_{t,r} = f_{t,r}^{0.54} \times 65 \times 10^{-6} \tag{10}$$

where $f_{t,r}$ is the axial tensile strength, α_t is the descending segment parameter of the constitutive curve, and $\varepsilon_{t,r}$ is the strain at the maximum tension stress.

The tension and compression damage variables (d_t and d_c) can be calculated as follows [60]:

$$d_t = 1 - \sqrt{\frac{\sigma_t}{E_c\varepsilon_t}} \tag{11}$$

$$d_c = 1 - \sqrt{\frac{\sigma_c}{E_c \varepsilon_c}} \tag{12}$$

They are used after the tension stress reaches its peak value and the end of linear response of the comprehension stress-strain curve, respectively. Table 1 lists the material parameters of concrete, grout, and grouting mortar used for FE simulations, while the input parameters for the CDP model are given in Table 2.

Table 1 Material details of concrete, grout, and grouting mortar (GM) [48].

Item	Cubic compressive strength f_c (MPa)	Axial compressive strength $f_{c,r}$ (MPa)	Axial tensile strength $f_{t,r}$ (MPa)	Elastic modulus E_c (MPa)
Concrete	39.8	26.62	2.64	32460
Grout	86.2	54.12	3.51	38424
GM	82.1	51.54	3.42	38129

Note: $f_{c,r}$, $f_{t,r}$, and E_c are calculated from f_c based on [58].

Table 2 Major plasticity material parameters for CDP model.

	Poisson's ratio, ν_c	Dilation angle, ψ	Flow potential eccentricity, e	f_{b0}/f_{c0}	Shape factor, k	Viscosity parameter
Concrete 1#	0.2	30	0.1	1.16	2/3	0.001
Concrete 2#	0.2	30	0.1	1.16	2/3	0.0005
Grout	0.2	30	0.1	1.16	2/3	0.0005
GM	0.2	30	0.1	1.16	2/3	0.0005

Note: f_{b0}/f_{c0} is the ratio of compression strength subjected to biaxial loading to uniaxial compression strength; Concretes 1# and 2# are adopted for the monolithic and precast samples, respectively.

2.4.2 Steel sleeves, reinforcing bars, and transition bars

The constitutive relationships for the steel sleeves and reinforcing bars are kept the same and described using a bilinear elastic-plastic model. The hardening modulus E_{h1} is equal to $0.01E_s$, where E_s is the initial elastic modulus (Fig. 3b). The Poisson's ratio for all the steel materials is taken as 0.3. Table 3 lists other mechanical parameters of reinforcing rebar, transition rebar, and steel sleeve adopted. In order to simulate the relative displacement and strain penetration between the transition rebar and grout (mortar) in an easier way, the post-yielding modulus of the transition rebar is deliberately reduced, as displayed in Fig. 3b; the detailed approach is to be presented next.

As the strain distribution at the transition rebar-grout interface is complicated and affected by a wide range of factors leading to the real strain distribution being difficult to measure, and the good interface bond between the transition bar and grout occurs in the small zone of the transition bar end, a useful assumption of uniform strain along the transition rebar in the gap and strain penetration

regions is made for simplification in this study, which has been also used by others to study the structural behaviour of grout-filled sleeves with acceptable accuracy [61-64]. As depicted in Fig. 4, the relationship between the average strain of the transition bar in the gap and strain penetration regions (ε_{u1}) and the total deformation of the transition bar (L_Δ) in relation to the entire length of the transition bar (L_t) can be expressed as:

$$\varepsilon_{u1} = \frac{L_\Delta}{\gamma L_t} \tag{13}$$

where γ is the modification coefficient of deformation length.

Table 3 Material properties of reinforcing rebar, transition rebar, and steel sleeve [48].

Item	Diameter (mm)	Area (mm^2)	f_y (MPa)	f_u (MPa)	E_s (GPa)
Stirrup	8	50.24	431	580	200
Longitudinal rebar	16	200.96	428	569	198
Transition rebar 1#	16	200.96	418	556	198
Transition rebar 2#	18	254.34	428	559	200
Steel sleeve	/	/	390	527	206

Note: f_y is the yield strength; f_u is the tension strength; E_s is the elastic modulus.

However, the relative displacement and strain penetration between the transition rebar and grout are rather difficult to simulate via finite element modelling directly. For simplicity, the perfect bond between the transition rebar and grout is assumed in the FE model, and the total deformation of the transition bar (L_Δ) is assumed concentrated in the small thickness of the grouting mortar (L_g). Thus, the corresponding strain of the transition bar in the grouting mortar area (ε_{u2}) can be expressed as:

$$\varepsilon_{u2} = \frac{L_\Delta}{L_g} \tag{14}$$

Substituting Eq. (13) into Eq. (14) gives:

$$\varepsilon_{u2} = \gamma \frac{L_t}{L_g} \varepsilon_{u1} \qquad (L_t \le 16 d_t + L_g) \tag{15}$$

where ε_{u1} can be calculated as:

$$\varepsilon_{u1} = \frac{f_u - f_y}{E_{h1}} + \varepsilon_y \tag{16}$$

Note that γ should be smaller than 1.0 but herein is taken as 1.0 to approximately compensate the restraining effect of the grouting mortar on the deformation of the transition rebar resulting from the perfect bond between the transition bar and grouting mortar in the FE model. In addition, the true stress-strain relationship is required for FE models. The true stress σ_T, true strain ε_T, and true plastic strain ε_p can be obtained as:

$$\sigma_T = \sigma_N (1 + \varepsilon_N) \tag{17}$$

$$\varepsilon_{\mathrm{T}} = \ln\left(1 + \varepsilon_{\mathrm{N}}\right) \tag{18}$$

$$\varepsilon_{\mathrm{p}} = \varepsilon_{\mathrm{T}} - \frac{\sigma_{\mathrm{T}}}{E_{\mathrm{b}}} \tag{19}$$

where σ_{N} and ε_{N} are the engineering stress and strain, respectively.

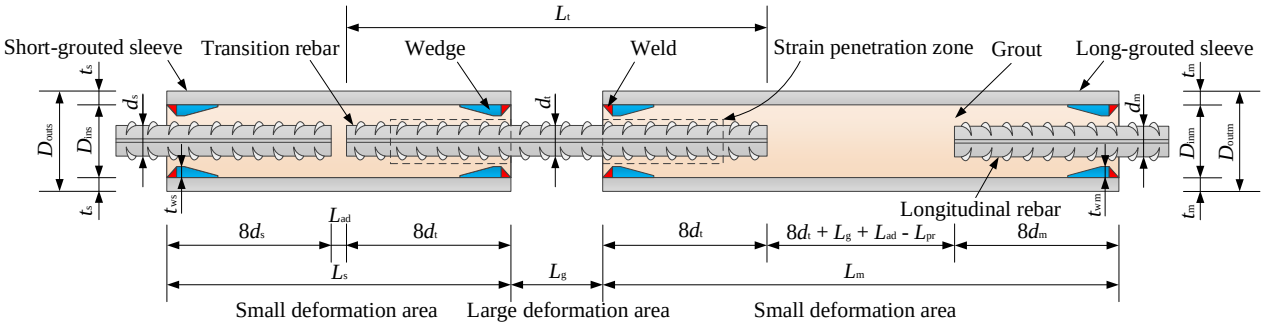

Fig. 4. Schematic diagram of the proposed double-grouted sleeve splice.

2.5 Boundary and loading conditions

To make the simulated boundary conditions of FE model as close as possible to those of the tested specimen, the displacements in X and Z directions as well as the rotations in Y and Z directions on the top of the column are restricted, and so are the displacements in X, Y, and Z directions as well as the rotations in Y and Z directions on the bottom of the column. The symmetrical boundary conditions are employed at the model to simulate the mechanical performance of the complete beam to column joint. The constant vertical load of 350 kN is initially imposed on the top surface of the prefabricated column for simulations, which is half the maximum experimental axial compression load of 700 kN. Subsequently, a monotonic displacement-based vertical loading is used on the top face of the loading plate to simulate the loading process of a hydraulic actuator used in experiments. The boundary and loading conditions for FE simulations are shown in Fig. 2. Details can be found in a previous study [48] about the sample preparation, test setup, instrumentation, and loading schemes.

3. Validation of finite element simulations

To the authors' best knowledge, so far, only an experimental study on the structural behaviour of the proposed novel joint with double-grouted couplers has been reported in the existing literature [48]. Therefore, the established FE model can only be validated using experimental results acquired from [48] in terms of load-deflection response at beam free end and failure modes, followed by a detailed analysis of stress distribution of the steel cages and sleeves.

3.1 Load-deflection response

Fig. 5 illustrates the simulated load-deflection response of beam-column joints in comparison with

experimental results. The average envelope of the experimental hysteretic curves is adopted for comparison given the significant distinction of the measured load-deflection curves in the push and pull directions. As seen, the simulated elastic stiffness by FE model is slightly greater than the experimental data, which can be explained by the fact that the stiffness change resulting from the cracking and crushing of concrete and grouting mortar is not considered in the material constitutive models and the bond between concrete and reinforcement is assumed to be perfect for FE modelling. Overall, there exists a satisfactory agreement between simulation and experimental results in terms of load-deflection curves. Table 4 lists the simulated and experimental yield and peak loads, indicating a good agreement between them with a discrepancy of only about 4% and 2%, respectively. Thus, the proposed FE model can be adopted to predict the load-carrying capacity of the joint with short and long couplers.

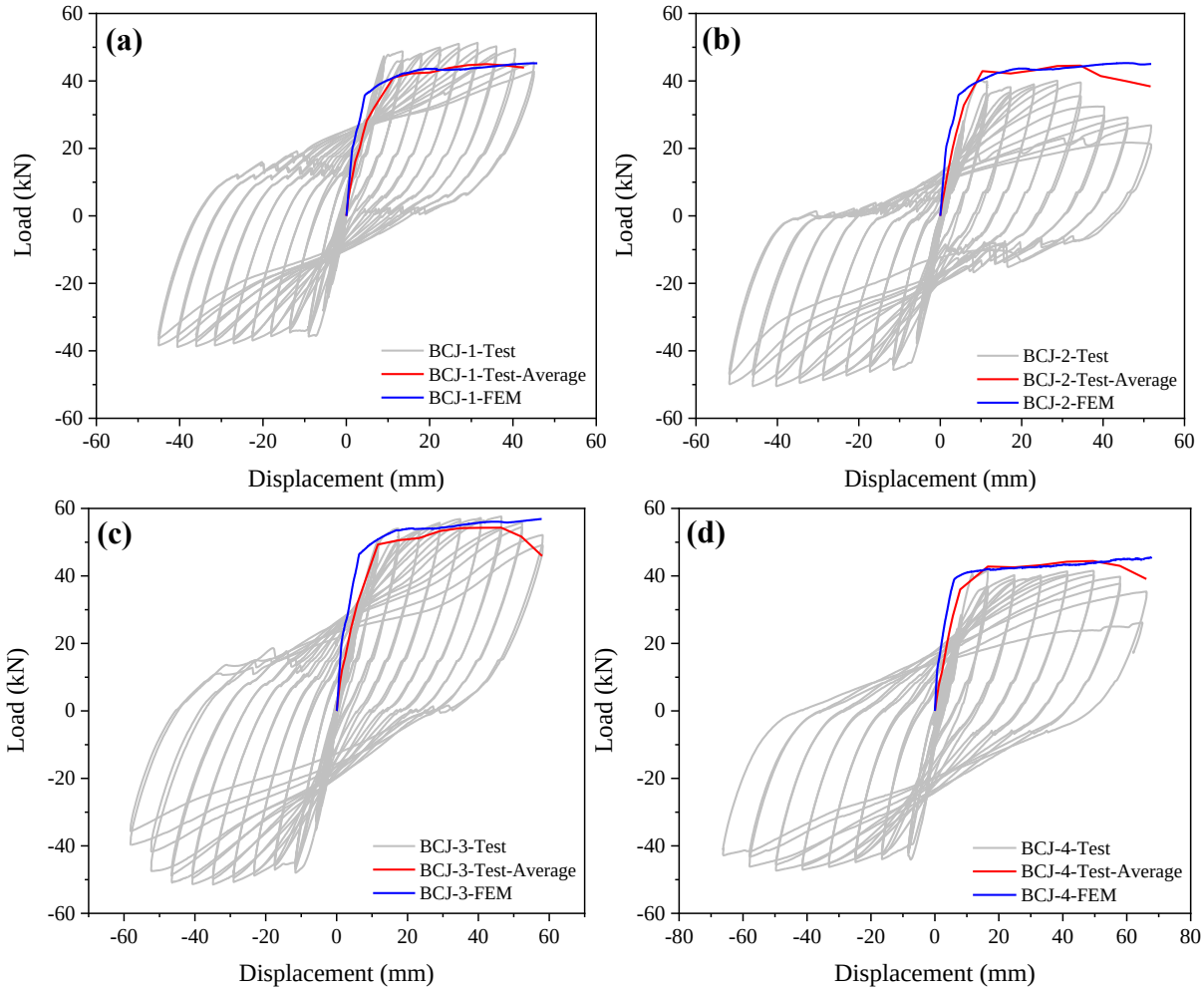

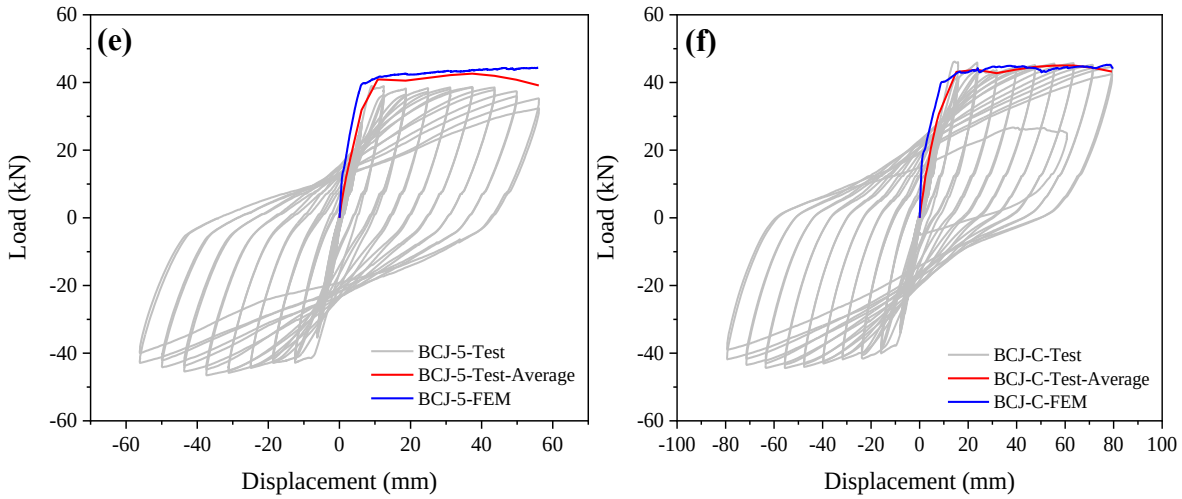

Fig. 5. Experimental and simulated load-displacement response of the specimens.

Table 4 Comparison between experimental and FE simulation data.

Specimen	Experimental result		Simulation result		Comparison	
	P_{ye} (kN)	P_{maxe} (kN)	P_{yn} (kN)	P_{maxn} (kN)	P_{ye}/P_{yn}	P_{maxe}/P_{maxn}
BCJ-1	33.89	44.98	35.77	45.24	0.95	0.99
BCJ-2	37.39	44.56	35.80	45.29	1.04	0.98
BCJ-3	44.27	54.28	46.33	56.89	0.96	0.95
BCJ-4	37.32	44.43	38.80	45.50	0.96	0.98
BCJ-5	35.87	42.62	38.98	44.38	0.92	0.96
BCJ-C	36.77	45.04	39.48	45.24	0.93	1.00
Mean					0.96	0.98
SD					0.04	0.02

Note: P_{ye} and P_{yn} are the experimental and simulated yield loads, respectively; P_{maxe} and P_{maxn} denote the experimental and simulated peak loads, respectively; SD is the standard deviation.

3.2 Failure modes

Although there is no mature tool in Abaqus available for demonstrating the cracks of the concrete, the tension and compression damage parameters can be approximately regarded as an indicator of cracking development [57]. Fig. 6 depicts the failure modes of the simulated and tested specimens. During the tests, obvious large tensile cracks for samples BCJ-1 to BCJ-3 and fine tensile cracks for samples BCJ-4 and BCJ-5 in the linking region were observed at the final failure stage, which can be also well found in the FE simulations. Both suggest that all the samples are subjected to a flexural failure mode at the beam end near prefabricated column face with the yielding of steel rebars and the crushing of concrete or both concrete and grouting mortar. The simulation results indicate that the grouted sleeves with higher stiffness and strength inhibit the propagating and widening of the cracks, which is consistent with the experimental results. In addition, the simulation results also illustrate the failure mechanism of a strong column and a weak beam followed by a stronger joint as no damage is

caused in the core zone of the joint.

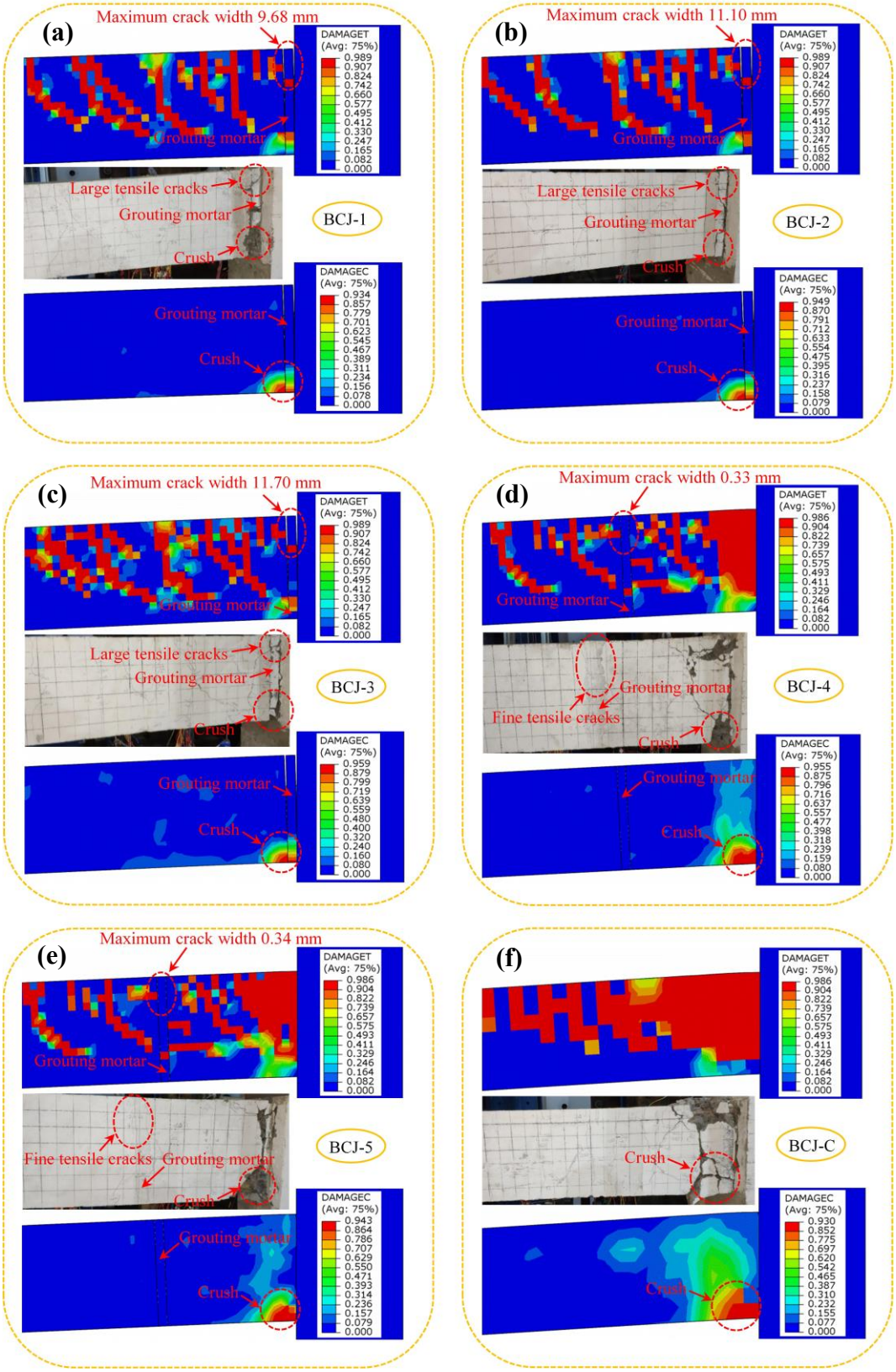

Fig. 6. Failure modes: experimental against FE simulation results.

As seen in Fig. 7, the damage of the grouting mortar in samples BCJ-1 to BCJ-3 is greater than that in samples BCJ-4 and BCJ-5. This is because the grouting mortar in samples BCJ-1 to BCJ-3 is arranged in the cross-section subjected to maximal flexural moment and the resistance in the regions

on both sides of the grouting mortar reinforced by grout-filled couplers is significantly higher than that of the grouting mortar. The above analyses imply that the developed FE model can be used to satisfactorily predict the failure modes and crack patterns of the precast beam-column joint with short and long sleeves.

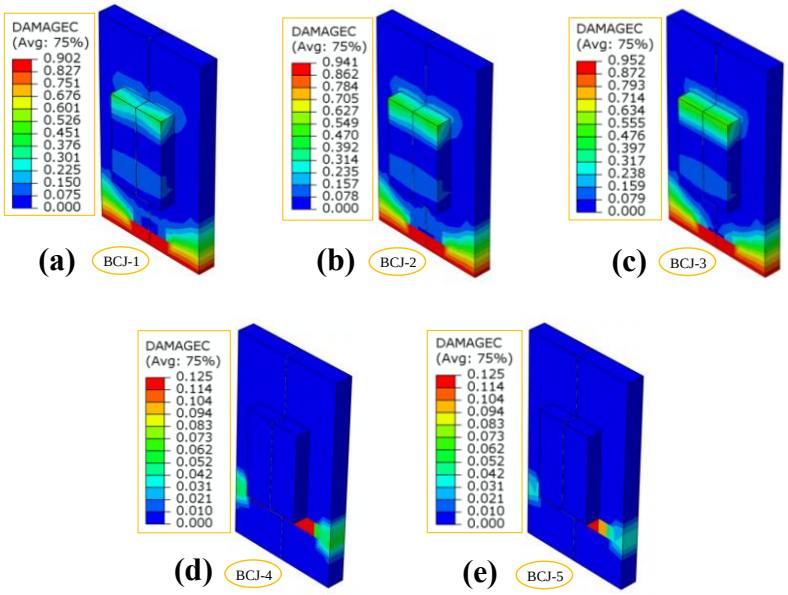

Fig. 7. Failure modes of grouting mortar.

3.3 Stress distribution

3.3.1 Steel cages

It is worth mentioning that the transition rebar was not attached with strain gauges as the strain gauges could make the transition rebar difficult to install. Thus, strain of the transition rebar was not measured during the experimental tests. Such limitation can be remedied by FE simulation. Although the assumption of the perfect bond between the transition reinforcement and grout can result in the strain/stress distributions of the transition rebars being different from the actual situation, the post-yielding modulus of the transition rebars is reduced to ensure that the simulated maximum stress of the transition bars is close to the actual situation. Therefore, the stress of the transition bars can be used for stress comparison and analysis. Fig. 8 shows the simulated Von-Mises stress distribution of the reinforcement cages at the end of loading. As seen in Fig. 8a and b, the stress of the joint anchorage rebars in samples BCJ-1 and BCJ-2 is very small (only approximately 70 MPa), attributing to the larger outer surface area of the short-grouted sleeve that provides a greater bond force between the concrete and sleeve compared to a steel bar. As the diameters of the top and bottom transition bars increase, the maximum stress of the joint anchorage bars goes up by 87% but is still very small (Fig.

8c). However, as the short-grouted sleeves are completely moved from the joint core area to the protruding beam, the maximum stress of the joint anchorage bars rises by around 700%, while the maximum stress of the transition bars declines obviously (Fig. 8a-e). The maximum stress of all the steel bars in specimens BCJ-1 and BCJ-2 is 15.1% and 15.3% greater than that in specimens BCJ-5 and BCJ-4, respectively, indicating that the linking location between the prefabricated column and beam has a significant effect on the ultimate stress of the steel bars. Even if the discontinuous distributed stress resulting from the higher stiffness of the couplers in the prefabricated specimens happens, the maximum stress of the steel bars in the prefabricated joint with a protruding beam can be similar to that in the cast-in-place counterpart as the maximum stress of all the bars in specimens BCJ-4 and BCJ-5 is only 4.4% higher than that in specimen BCJ-C (Fig. 8d-f).

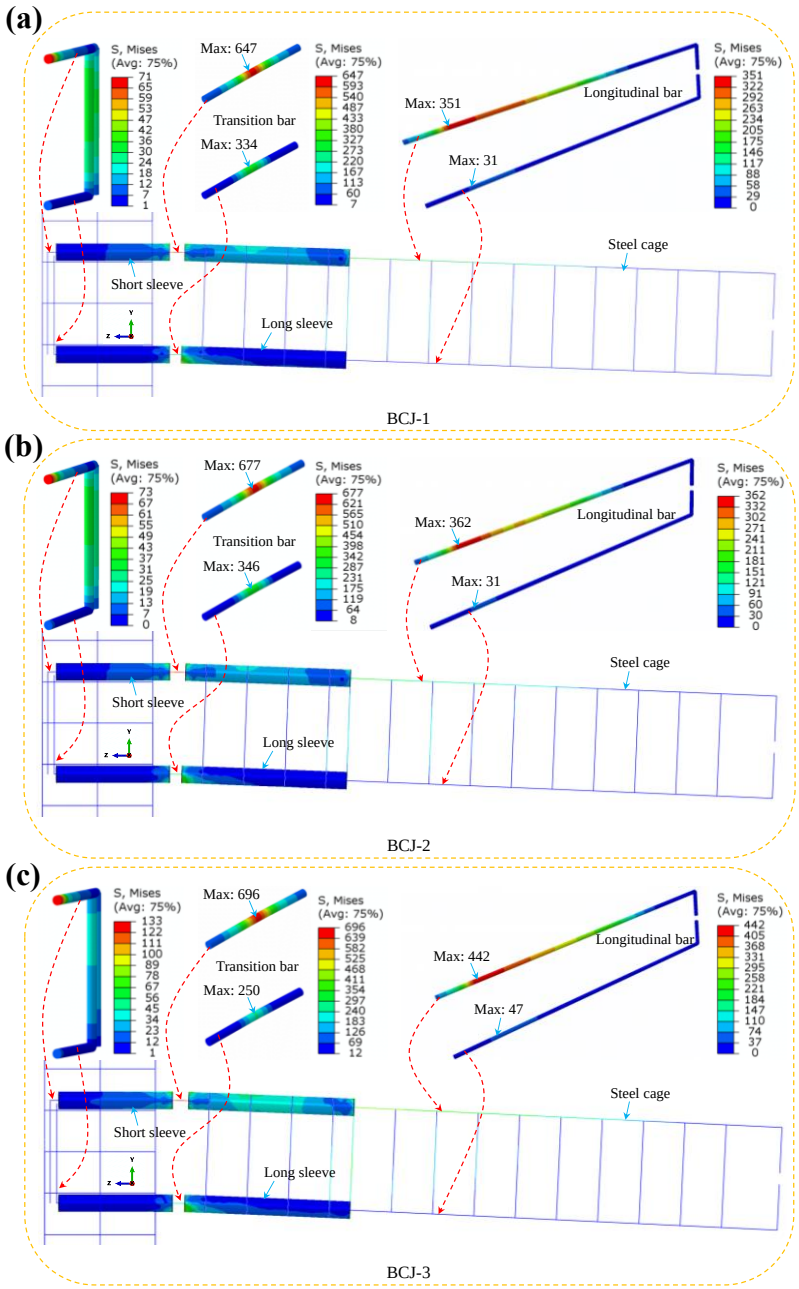

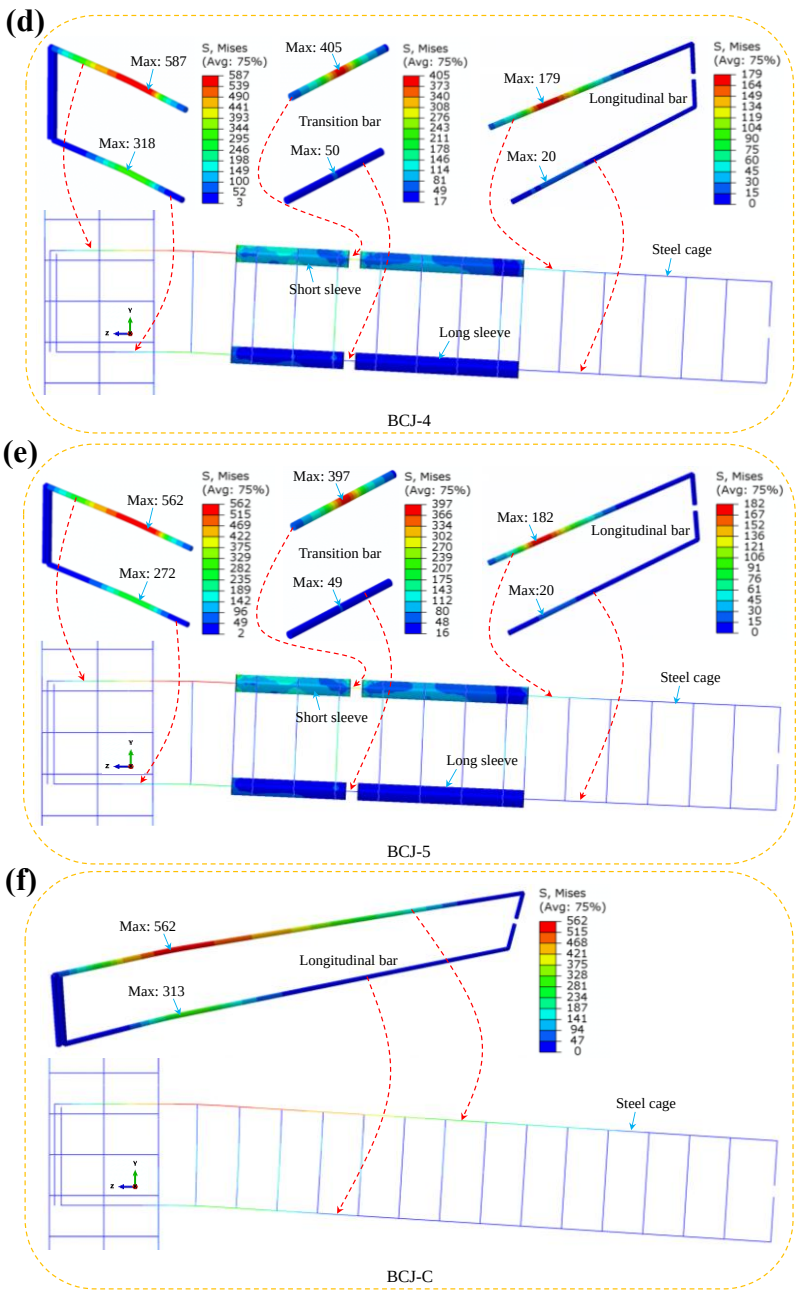

Fig. 8. Von-Mises stress distribution of reinforcement cages in specimens (in MPa).

3.3.2 Steel sleeves

Fig. 9 presents the simulated stress distribution of the steel sleeves. It can be seen that the maximal stress of all the sleeves is less than 390 MPa, indicating that the steel sleeves do not yield and can meet the strength requirement. The maximum stress of the sleeves in sample BCJ-3 is 18.4 % greater than that in sample BCJ-1, implying that the design parameters of the short and long steel sleeves used in the developed joint should match the tensile capacity of the linking bars (Fig. 9a and c). For samples BCJ-1 to BCJ-3 with no protruding beam, the maximum stress occurs in the long sleeve, while for samples BCJ-4 and BCJ-5 with a protruding beam length of 425 mm, the maximum stress exists in the short sleeve. Accordingly, the protruding beam significantly affects the stress distribution

of the short and long sleeves, which should be considered when designing the joint.

Overall, the finite element modelling can provide insight into the key results that cannot be acquired by limited experimental investigations. The above analyses show that the proposed FE model is dependable and thus can be employed for parametric studies to explore the effects of some key parameters on the mechanical behaviour of the proposed prefabricated beam-column joint.

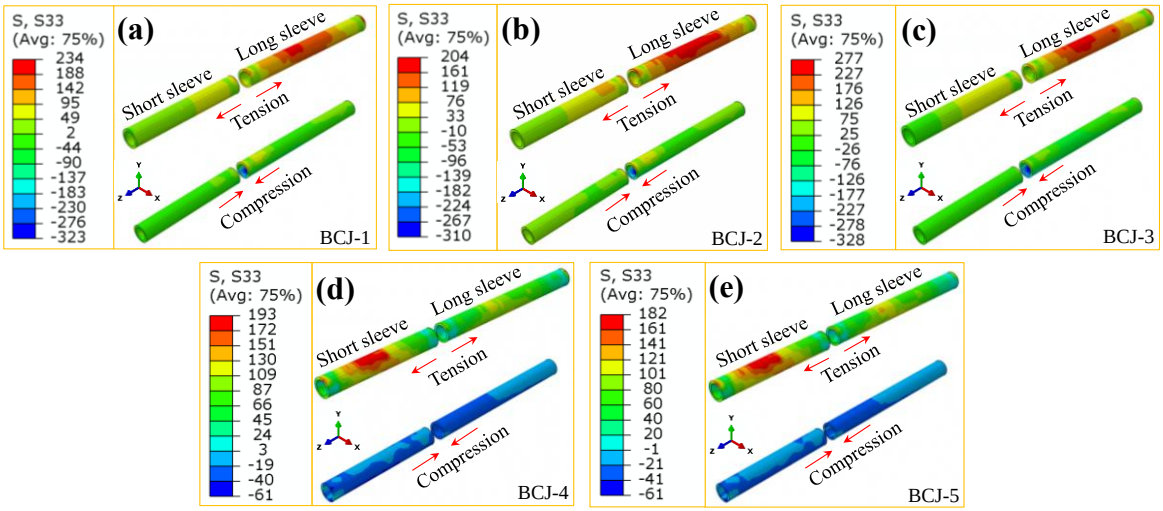

Fig. 9. Stress distribution of grouted sleeves in specimens (in MPa).

4. Parametric analysis

Based on the prototypes BCJ-1 and BCJ-5 that represent two different types of joints (i.e., with or without a protruding beam), FE models are established to study the influences of different factors on the structural behaviour of the prefabricated beam-column connection with double-grouted couplers, including length of protruding beam, thickness of grouting mortar, strengths of grouting mortar and precast concrete, diameter of rebar, and eccentricity of transition rebar.

4.1 Effect of protruding beam length

4.1.1 Load-deflection response

To investigate the effect of the protruding beam on mechanical performance of the developed joint, FE models with a wide range of protruding beam lengths from 137.5 mm (i.e., half the short sleeve length) to 525 mm (i.e., 1.5 times the prefabricated beam height) are developed. Fig. 10a displays the simulated load-deflection response at beam free end for specimens with various protruding beam lengths. The initial stiffness is almost not affected by the length of the protruding beam, whereas with the rise of loading before yielding, the rate of stiffness decline is enhanced with increasing protruding beam length (Figs. 10a and 11b). The yield load of specimen with a protruding beam length of 137.5 mm is the smallest, while as the length of the protruding beam reaches the short-grouted sleeve length

of 275 mm, the yield load achieves the largest. However, the further rise in protruding beam length does not lead to an obvious change in the yield bearing capacity of the joint. As the protruding beam length increases, the peak load and the second secant stiffness go up first but then drop (Figs. 10a and 11 b). In addition, as seen in Fig. 10a, the specimen with the protruding beam length being the same as the length of the short-grouted sleeve achieves the highest ultimate load-bearing capacity compared to other models.

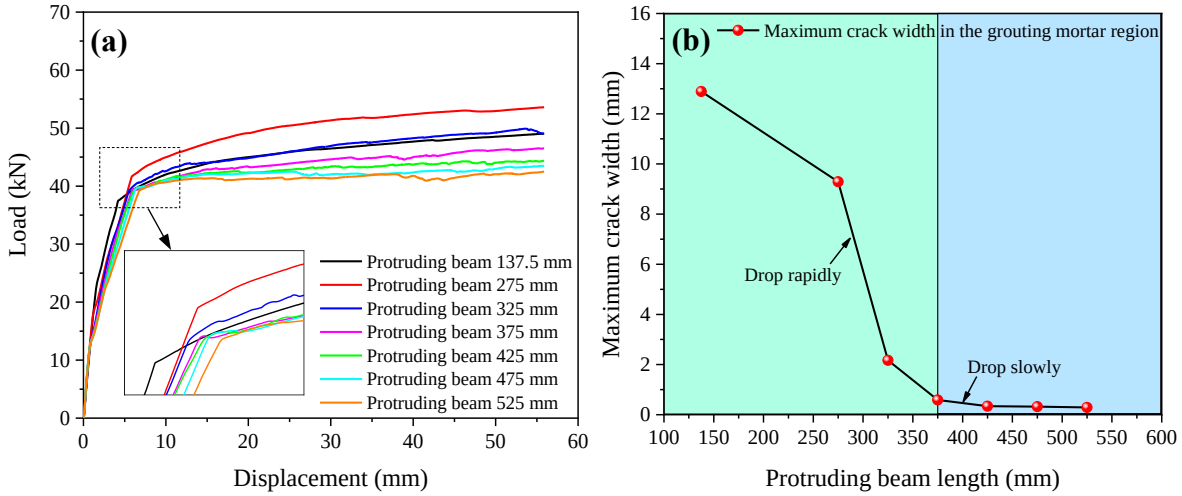

Fig. 10. Simulation results for specimens with different protruding beam lengths: (a) load-displacement response; (b) maximum crack width in the grouting mortar region.

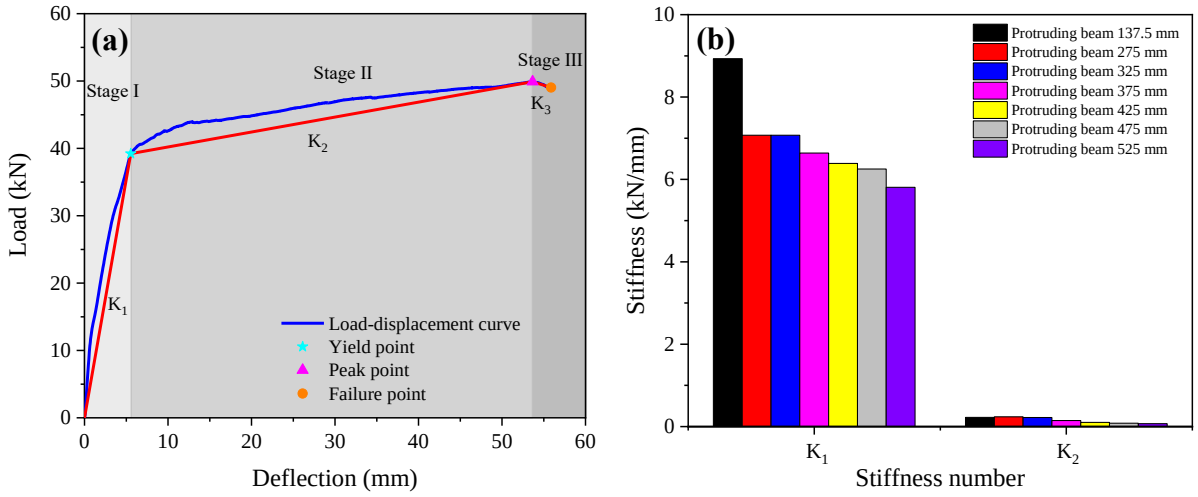

Fig. 11. Simulated secant stiffness for specimens: (a) schematic diagram; (b) with different protruding beam lengths.

4.1.2 Failure modes

Fig. 12 illustrates the final failure modes of samples with various protruding beam lengths. The compression damage of the models primarily occurs at the grouting mortar area. The tension cracks in the grouting mortar region of the specimens are significantly wider than those in other specimens with a protruding beam length smaller than that of the short-grouted sleeve, i.e., 275 mm. However,

as the protruding beam length increases, the compression crushing is transferred from the grouting mortar region to the beam end near column face and the range of the tension damage goes up. Moreover, with the rising protruding beam length, the maximum crack width in the linking region drops rapidly first when the protruding beam length is smaller than 375 mm (i.e., approximately 1.36 times the short sleeve length), and then drops slowly afterwards (Fig. 10b). These indicate that the short sleeve length should be carefully considered when designing the protruding beam.

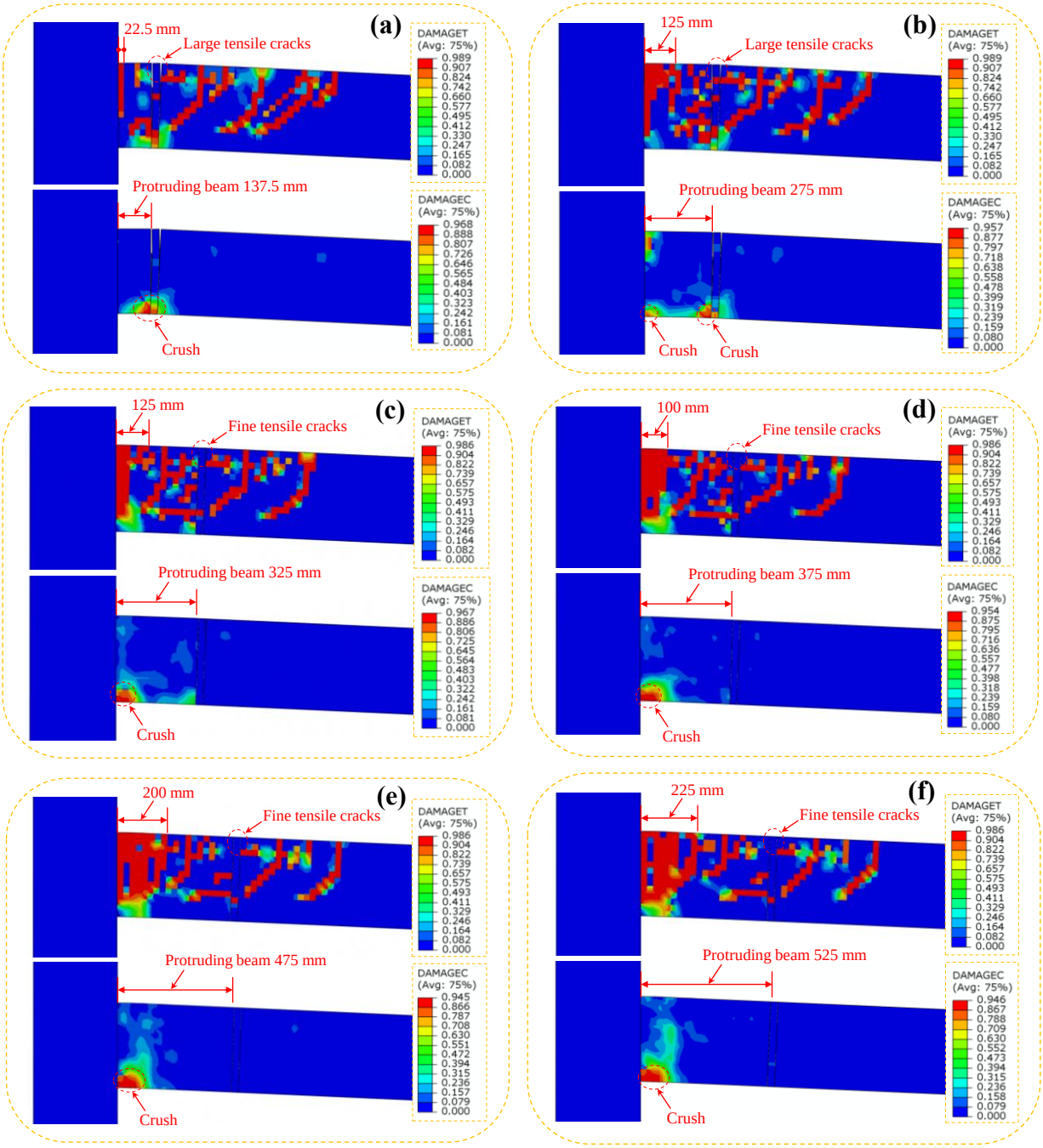

Fig. 12. Failure modes of the joints with various protruding beam lengths.

4.2 Effect of grouting mortar thickness

According to the experimental observations, the damage of the grouting mortar in specimens with no

protruding beam was greater than that with a protruding beam. Thus, FE models for specimens with grouting mortar thicknesses from 30 mm to 110 mm based on the prototype BCJ-1 are established to explore the effect of grouting mortar thickness on mechanical behaviour of the proposed joint. Fig. 13a depicts the simulated load-displacement response at beam free end for specimens with various grouting mortar thicknesses. With the rising grouting mortar thickness, the stiffness before yielding gradually declines, while the yield load and corresponding displacement slightly increase. This can be explained by the fact that the increased deformation capacity in the grouting mortar region resulting from the enhanced elongation capacity of the transition bar helps increase the yield deflection and reduce the stiffness, and the yielding of the transition rebar is delayed as its length increases, leading to an enhanced yield load. The peak load slightly reduces first and then slightly goes up with the rising grouting mortar thickness when the grouting mortar thickness is smaller and greater than 50 mm, respectively. As seen in Fig. 13b, as the grouting mortar thickness goes up, the maximum stress of the tension transition rebar declines rapidly first and then slowly when the grouting mortar thickness is smaller and greater than 50 mm, respectively. However, a greater tension damage of the grouting mortar gradually takes place with the increase of the grouting mortar thickness (Fig. 14).

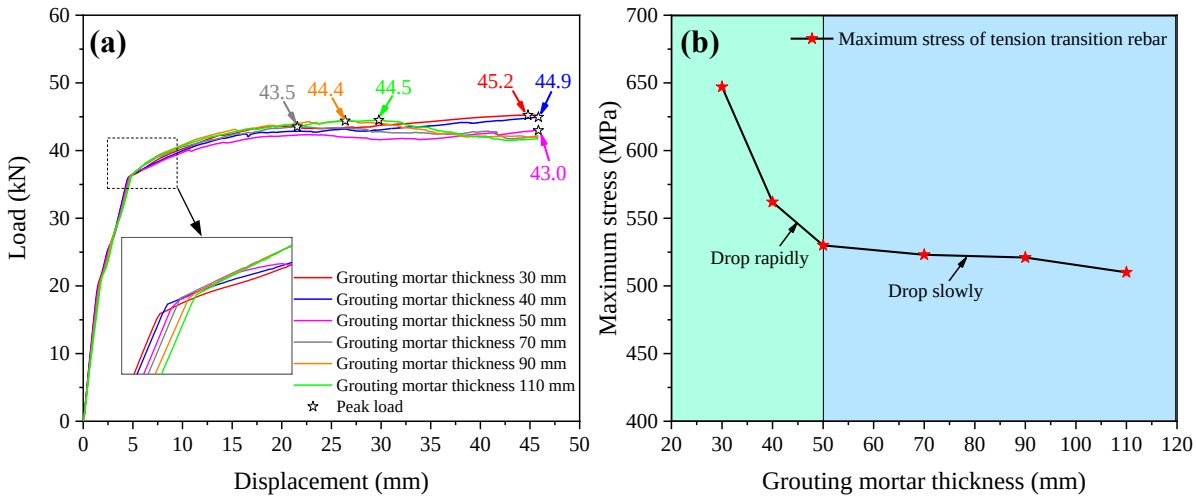

Fig. 13. Simulation results for specimens with different grouting mortar thicknesses: (a) load-displacement response; (b) maximum stress of the tension transition rebar.

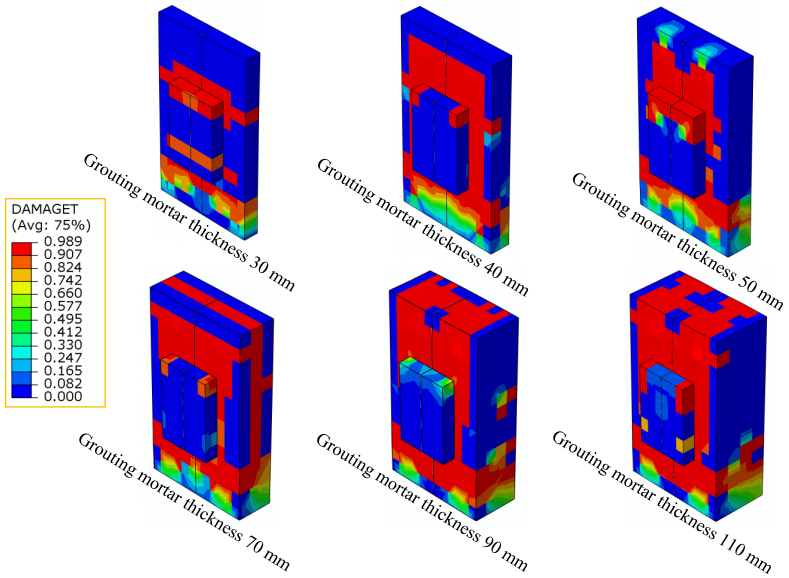

Fig. 14. Failure modes of grouting mortar in specimens with various grouting mortar thicknesses.

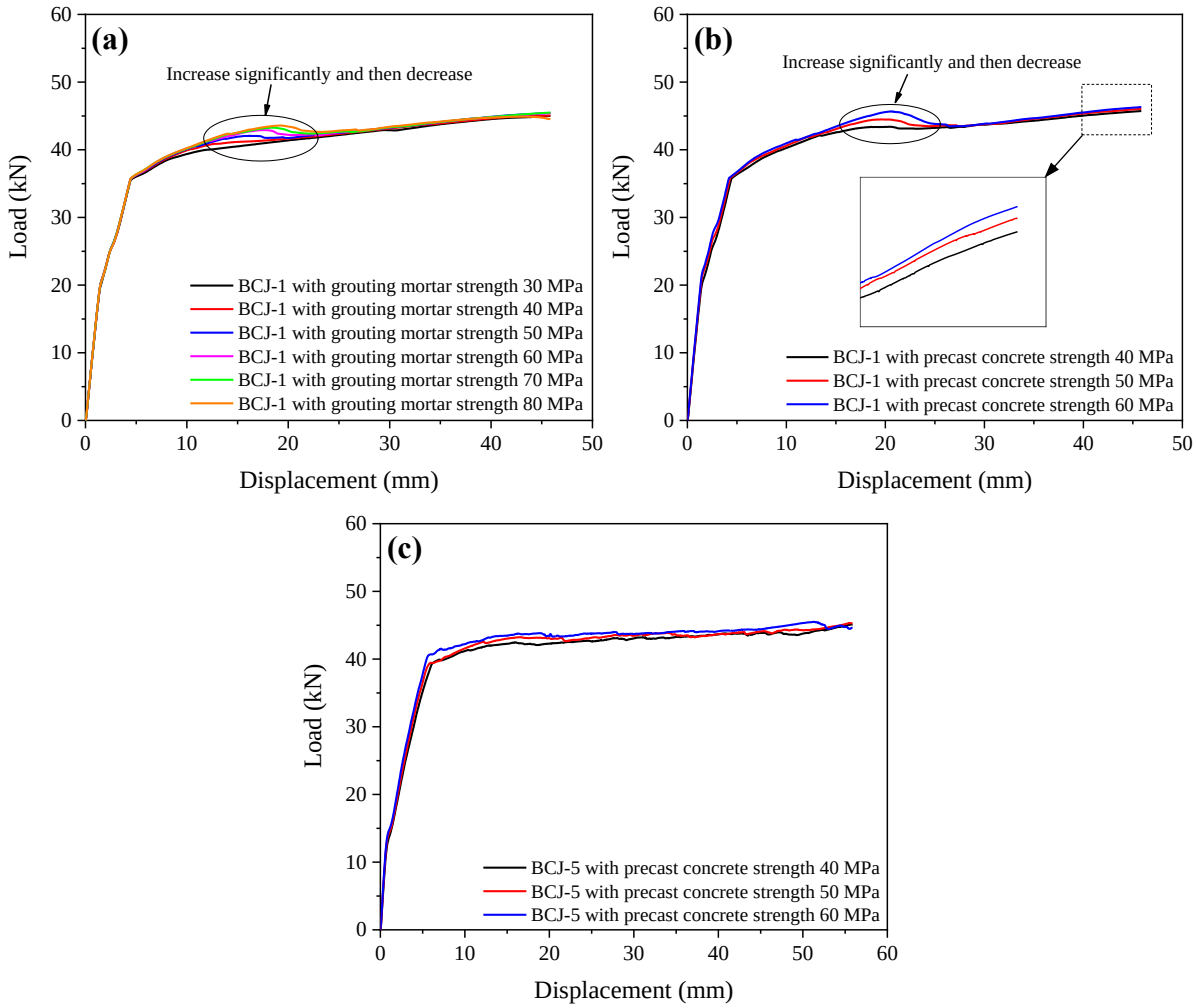

Fig. 15. Load-displacement response for specimens: (a) BCJ-1 with various grouting mortar strengths; (b) BCJ-1 with various precast concrete strengths; (c) BCJ-5 with various precast concrete strengths.

4.3 Effect of grouting mortar and precast concrete strengths

FE models for specimens with cubic concrete strengths varying from 30 MPa to 80 MPa for grouting mortar and from 40 MPa to 60 MPa for precast concrete are investigated. Only the prototype BCJ-1 with no protruding beam is adopted to study the impact of grouting mortar strength on mechanical behaviour of the joint because the grouting mortar in specimen BCJ-1 is placed in the critical zone with maximal flexural moment. As seen in Fig. 15a and b, with the rising strength of the grouting mortar or precast concrete, the load-bearing capacity of specimens goes up after yielding and then drops, while the change only occurs in the local zone of the load-displacement curves. This indicates that increasing the strength of the grouting mortar or precast concrete has a limited influence on the load-carrying capacity of the connection without a projecting beam. However, when the double-grouted sleeve splice is far away from the beam end near column face, no obvious change can be found in the local region of the load-displacement curves and the rise in precast concrete strength for the joint with a protruding beam leads to a slight enhancement in the load-bearing capacity (Fig. 15c).

Table 5 Details of the specimens with different diameters of rebar for simulations.

Model ID	d_{ju} (mm)	d_{jl} (mm)	d_{tu} (mm)	d_{tl} (mm)	P_{yn} (kN)	Δ_{yn} (mm)	P_{maxn} (kN)	Δ_{maxn} (mm)	P_e (kN)	P_c (kN)	P_e/P_{maxn}	P_c/P_{maxn}
BCJ-1-JU16-TU16	16	16	16	16	35.77	4.45	45.24	44.81	42.63	42.63	0.94	0.94
BCJ-1-JU16-TU18	16	16	18	16	45.30	6.12	55.32	44.35	53.95	53.95	0.98	0.98
BCJ-1-JU16-TU20	16	16	20	16	55.61	8.10	62.34	45.84	66.61	65.19	1.07	1.05
BCJ-5-JU16-TU16	16	16	16	16	38.98	6.01	44.38	55.88	43.63	43.63	0.98	0.98
BCJ-5-JU16-TU18	16	16	18	16	38.70	5.91	44.46	55.86	43.63	43.63	0.98	0.98
BCJ-5-JU16-TU20	16	16	20	16	38.90	5.85	44.61	55.88	43.63	43.63	0.98	0.98
BCJ-5-JU18-TU16	18	16	16	16	48.18	7.50	53.98	54.26	55.22	55.22	1.02	1.02
BCJ-5-JU18-TU18	18	16	18	16	48.50	7.53	54.44	52.46	55.22	55.22	1.01	1.01
BCJ-5-JU20-TU16	20	16	16	16	48.25	6.86	61.44	48.53	68.17	63.34	1.11	1.03
BCJ-5-JU20-TU18	20	16	18	16	59.19	9.42	62.98	55.88	68.17	68.17	1.08	1.08
BCJ-5-JU20-TU20	20	16	20	16	59.18	9.19	63.02	53.00	68.17	68.17	1.08	1.08
Mean											1.02	1.01
SD											0.06	0.05

Note: d_{ju} is the diameter of upper tension joint anchorage bar; d_{jl} is the diameter of lower compression joint anchorage bar; d_{tu} is the diameter of upper tension transition rebar; d_{tl} is the diameter of lower compression transition bar.

4.4 Effect of rebar diameter

To investigate the effect of the transition and joint anchorage bars on mechanical behaviour of the precast beam-column joint connected using short and long sleeves, 11 FE models for specimens with various diameters of the tension transition and tension joint anchorage bars are developed, the details of which are given in Table 5. For labels, BCJ-1-JU16-TU16 (reference model) and BCJ-5-JU16-

TU16 (reference model), “BCJ-1” and “BCJ-5” stand for the joint with no protruding beam and with a protruding beam length of 425 mm, respectively, “JU16” represents the tension joint anchorage rebar diameter of 16 mm, and “TU16” denotes the tension transition bar diameter of 16 mm. It is worth noting that three different diameters (i.e., 16 mm, 18 mm and 20 mm) for the tension transition and tension joint anchorage bars are considered for FE simulations because they are located in the critical areas in the joint. However, owing to the smaller stress on the joint anchorage bars resulting from the good bond behaviour between the short sleeve and precast concrete for specimen BCJ-1, the influence of the diameter of the joint anchorage bar for the specimen BCJ-1 is not taken into account in this study.

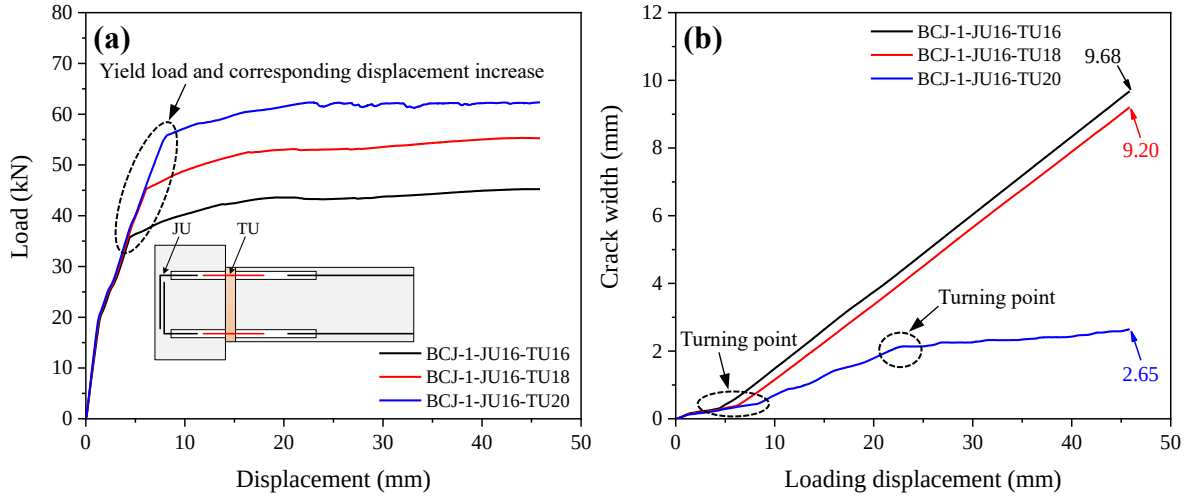

Fig. 16. Simulation results for BCJ-1 with various diameters of tension transition rebar: (a) load-displacement response; (b) grouting mortar crack width-loading displacement curves.

4.4.1 For specimen BCJ-1

Fig. 16a displays the load-displacement curves at beam free end for specimen BCJ-1 with various diameters of the tension transition rebar. Increasing the tension-transition-rebar diameter results in a continuous enhancement in yield and ultimate loads of the joint. As the tension-transition-rebar diameter increases from 16 mm to 20 mm, the yield and ultimate load-bearing capacity goes up by 55.5% and 37.8%, respectively (Table 5). This indicates that the transition bar diameter has a significant impact on the load-carrying capacity of the joint without a projecting beam. Fig. 16b presents the grouting mortar crack width-loading displacement curves for specimen BCJ-1 with various diameters of the tension transition rebar. It can be found that the grouting mortar crack width-loading displacement curve for specimen BCJ-1-JU16-TU20 is obviously different from those for specimens BCJ-1-JU16-TU16 and BCJ-1-JU16-TU18. There exist two turning points in the curve for

specimen BCJ-1-JU16-TU20. With the increase of the tension-transition-rebar diameter from 16 mm to 18 mm, the maximum crack width only declines by 0.48 mm, while as its diameter goes up from 16 mm to 20 mm, the maximum crack width drops by 7.03 mm, which is 72.6% smaller than that of specimen BCJ-1-JU16-TU16.

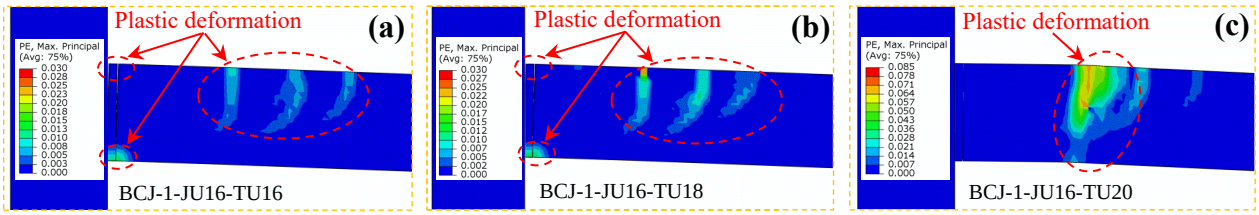

Fig. 17. Plastic strain distribution for specimen BCJ-1 with various diameters of tension transition rebar.

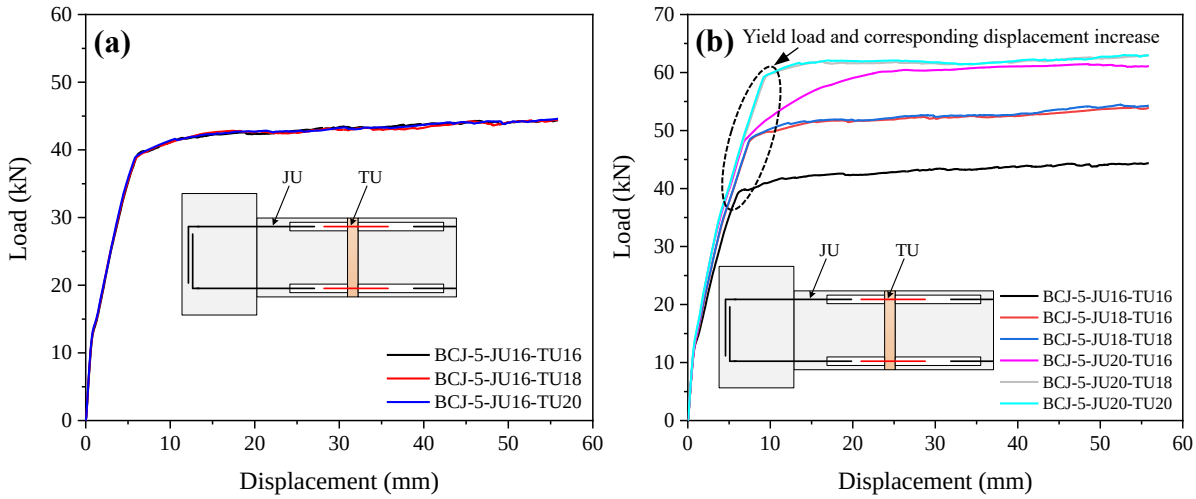

Fig. 18. Load-displacement response for specimen BCJ-5 with various diameters of tension transition rebar and tension joint anchorage rebar.

It can be ascribed to the distribution of the plastic strain components, as depicted in Fig. 17. The plastic deformation of specimen BCJ-1-JU16-TU18 is similar to that of specimen BCJ-1-JU16-TU16. Their plastic deformations are primarily concentrated in the two ends of the long-grouted sleeve (Fig. 17a and b). However, unlike specimens BCJ-1-JU16-TU16 and BCJ-1-JU16-TU18, the concentration of plastic deformation of specimen BCJ-1-JU16-TU20 is primarily located at the end of the long-grouted sleeve near the side of loading point and no significant plastic damage occurs in the grouting mortar region. This is because the moment capacity in the grouting mortar region is obviously greater than the moment demand when the tension-transition-bar diameter increases from 16mm to 20 mm, resulting in the moment control cross-section being transferred from the grouting mortar region to the end of the long coupler near the side of loading point. Consequently, the damage locations and failure modes of the joint with no protruding beam can be controlled by changing the diameter of the tension

transition bar.

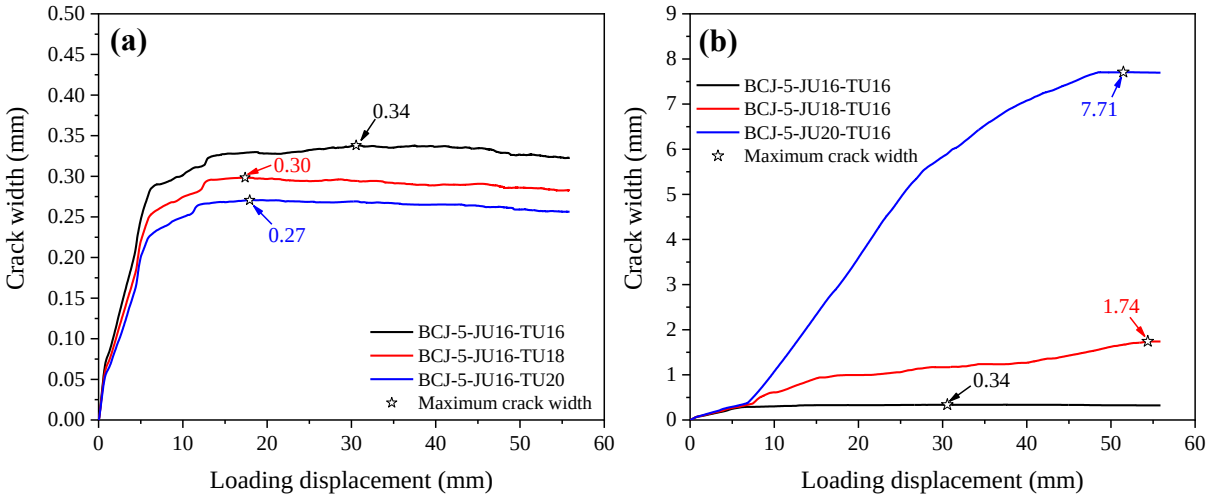

Fig. 19. Grouting mortar crack width-loading displacement curves for specimen BCJ-5 with various diameters of tension transition rebar and tension joint anchorage rebar.

4.4.2 For specimen BCJ-5

Figs. 18 and 19 respectively display the load-displacement response at beam free end and grouting mortar crack width-loading displacement curves for specimen BCJ-5 with various diameters of the tension transition rebar and tension joint anchorage rebar. As seen in Figs. 18a and 19a, a rise in the diameter of the tension transition rebar in specimen BCJ-5 almost has no influence on the load-deflection response but can slightly reduce the maximum crack width in the grouting mortar region which declines by 0.07 mm when the tension linking rebar diameter increases from 16 mm to 20 mm. This is because the tension transition rebar is far away from the beam end near column face, as a result of which increasing the tension linking rebar diameter for the joint with a projecting beam does not change its load-deflection response. However, rising the diameter of the tension joint anchorage bar not only significantly enhances the load-carrying capacity and stiffness, but also obviously increases the maximal crack width in the grouting mortar zone which goes up by 7.37 mm with the increase of tension joint anchorage bar diameter from 16 mm to 20 mm (Figs. 18b and 19b).

As given in Table 5, the yield and maximum loads of specimen BCJ-5-JU18-TU16 are 23.6% and 21.6% greater than specimen BCJ-5-JU16-TU16, respectively, while the yield and maximum loads of specimen BCJ-5-JU20-TU16 are 0.1% and 13.8% greater than specimen BCJ-5-JU18-TU16, respectively. This suggests that a continuous increase in the diameter of the tension joint anchorage bar in specimen BCJ-5 cannot continuously improve its yield load unless the diameter of the tension transition rebar increases simultaneously as the yield and maximum loads of specimen BCJ-5-JU20-

TU18 are 22.9% and 16.7% greater than specimen BCJ-5-JU18-TU16. The plastic strain distribution for specimen BCJ-5 with various diameters of the tension transition rebar and tension joint anchorage rebar is shown in Fig. 20. The plastic deformation of all samples is primarily concentrated in the area in the beam end near column face, suggesting that the rise in tension joint anchorage bar diameter does not completely transfer the damage location from the beam end near column face to the linking region. Hence, the damage locations and failure modes of the joint with a protruding beam cannot be completely controlled by only changing the tension joint anchorage bar diameter. Note that changing the diameter of the bars can essentially alter their tension capacity. As a result, as an alternative, the strength grade of rebar can be also used to adjust the mechanical performance of the connection.

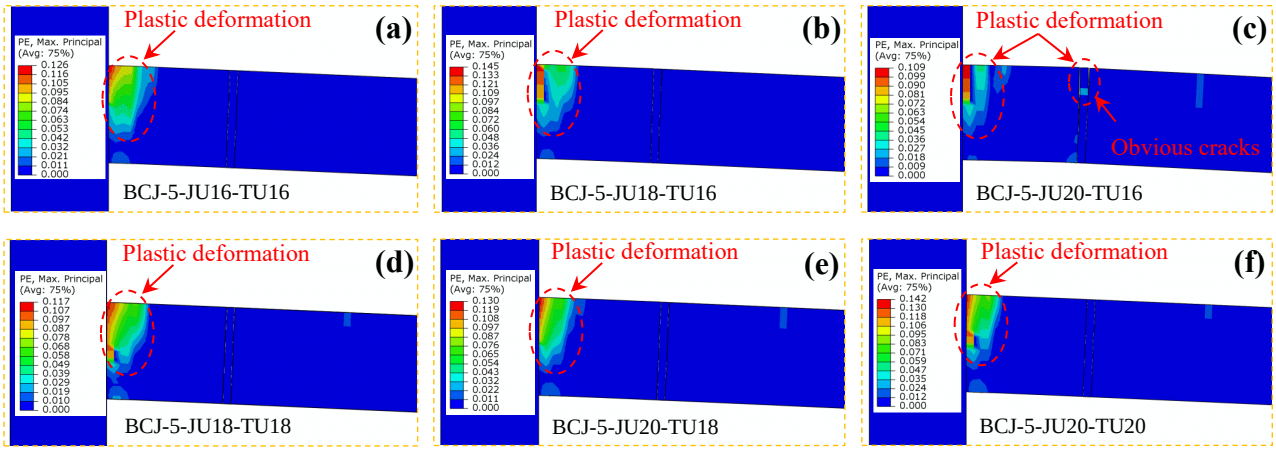

Fig. 20. Plastic strain distribution for specimen BCJ-5 with various diameters of tension transition rebar and tension joint anchorage rebar.

4.5 Effect of transition rebar eccentricity

4.5.1 Load-deflection response

According to Xu et al. [65], an eccentricity of embedded bar resulting from construction errors may occur in the grouted sleeve and its influences should be considered, while the study was only focused on the single-grouted sleeve splices. The effect of rebar eccentricity on mechanical performance of the structural components with double-grouted sleeves is still unclear. Thus, the influence of eccentricity of the tension transition rebar in the short and long sleeves is explored here. Note that although the eccentricity of the transition rebar may result in a decrease in the tensile strength of the double-grouted sleeve splice itself, it is not considered in the FE model due to a lack of relevant experimental results. An experimental study is required to systematically explore the effect of the eccentricity of the transition rebar on the tensile strength of the double-grouted sleeve splice. Fig. 21 shows the load-displacement response at beam free end with the tension transition rebar being

eccentric to the top or bottom of the inner wall of the grouted sleeves (i.e., with an eccentric distance of 8 mm). As seen in Fig. 21a, the upward eccentricity increases the ultimate load-carrying capacity of sample with no protruding beam by 3.3%, while the downward eccentricity declines its ultimate load-bearing capacity by 2.8%. The reason for this is that the control cross-section of load-carrying capacity is located in the linking region with the transition rebar and the change of force arm resulting from the off-centre of the tension transition rebar leads to a change of resistance of cross-section. However, the eccentricity of the tension transition rebar almost does not affect the load-bearing capacity of specimen with a protruding beam (Fig. 21b), as the grouting mortar region with the tension transition rebar is far away from the control cross-section of load-bearing capacity.

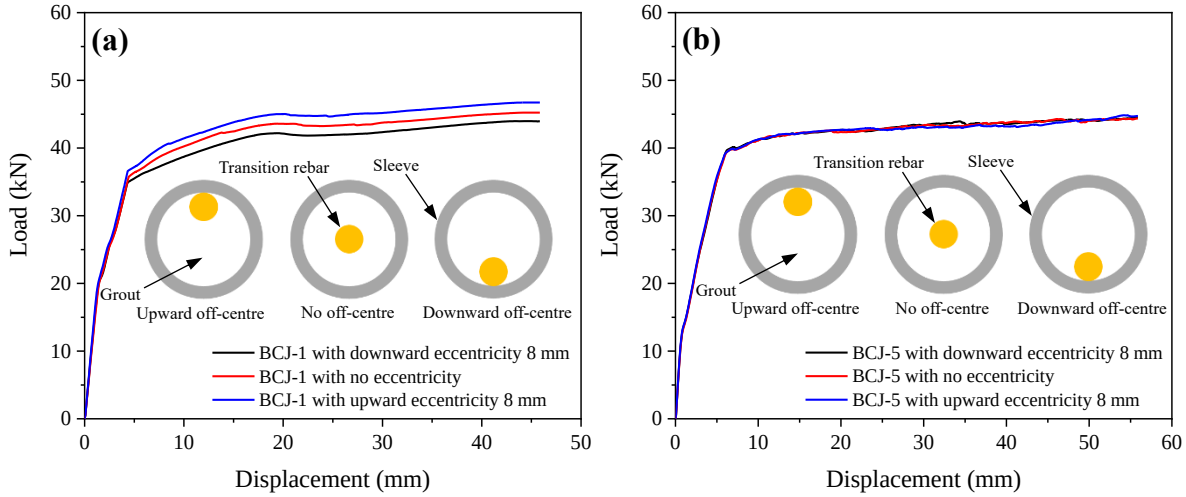

Fig. 21. Load-displacement response for specimens with various eccentricity of tension transition rebar: (a) BCJ-1; (b) BCJ-5.

4.5.2 Crack width in grouting mortar region

The grouting mortar crack width against loading displacement curves for the joint with eccentricity of the tension transition rebar are plotted in Fig. 22. For BCJ-1, the downward and upward eccentricity increases and declines the maximum crack width in the grouting mortar zone by 0.13 mm and 0.08 mm, respectively (Fig. 22a), while for BCJ-5, the downward and upward eccentricity rises and reduces the maximum crack width in the grouting mortar region by 0.04 mm and 0.13 mm, respectively (Fig. 22b). This indicates that whether the joint has a protruding beam or not, the downward and upward eccentricity can result in an increase and decrease of the crack width in the linking region, respectively and the protruding beam can reduce the negative impact of eccentricity of the transition rebar because the increment of the maximum crack width for the joint with a protruding beam is 69.2% lower than that with no protruding beam. This can be also ascribed to the

change of force arm resulting from the eccentricity of the tension transition rebar causing the change of deformation capacity of the grouting mortar region. Consequently, the eccentricity of the transition rebar has an impact on the mechanical performance of the prefabricated beam-column connection, which should be considered in design and construction.

In summary, compared with other parameters, the diameters of steel bars including transition rebar and joint anchorage rebar can be regarded as the most influential parameter because they have a great influence on the overall behaviour of the proposed joint, comprising load-bearing capacity, crack width in the linking region, damage location, and failure mode. Therefore, rebar diameters located in different segments of the joint should be carefully designed to achieve intended design purposes.

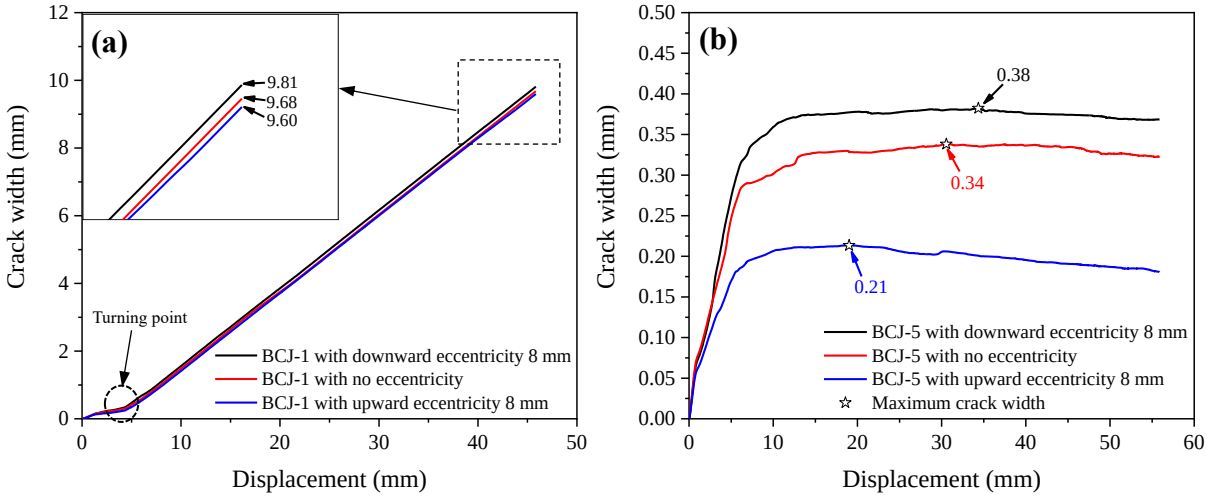

Fig. 22. Grouting mortar crack width-loading displacement curves for specimens with various eccentricity of tension transition rebar: (a) BCJ-1; (b) BCJ-5.

5. Theoretical predictions of load-bearing capacity

Herein, the load-bearing capacity of the proposed beam-column connection with various diameters of rebar is theoretically predicted and compared with simulation results presented in Section 4.4. The developed beam-column connection can be regarded as an emulative cast-in-place counterpart. Therefore, based on the common bending capacity calculation approach for cast-in-place flexural members [58], the bending capacity of the beam (M_{pr}) at different cross-sections can be easily calculated. Since the beam can be divided into different segments due to the presence of the short and long sleeves, which results in the fact that the moment capacity of different cross-sections may be varied to achieve certain design purposes. As a result, the existing calculation method based on the cross-section of the maximum bending moment cannot be directly used to calculate the load-bearing capacity of the proposed beam-column joint, and the failure control cross-section needs to be properly

determined. Hence, in this study, the method for determining the failure control cross-section is developed. It should be mentioned that the strength of the grouted sleeve region is significantly higher than that of the zone reinforced with steel rebars, indicating that the failure control cross-section only exists in the part reinforced with rebars. A schematic diagram of the failure control cross-section is given in Fig. 23.

Regarding the precast beam-column joint with no protruding beam, it is assumed that the moment demand of cross-section C-C (M'_{C}) is equal to its moment capacity (M_{C}). Therefore, the moment demand of cross-section E-E (M'_{E}) can be described as:

$$M'_{\mathrm{E}} = \frac{L_{\mathrm{e}}}{L_{\mathrm{c}}+L_{\mathrm{d}}+L_{\mathrm{e}}} M_{\mathrm{C}} \tag{20}$$

If $M_{\mathrm{E}} > M'_{\mathrm{E}}$, the failure is governed by the cross-section C-C (Fig. 23a), and the load-carrying capacity (P_{c}) can be obtained as:

$$P_{\mathrm{c}} = \frac{M_{\mathrm{C}}}{L_{\mathrm{c}}+L_{\mathrm{d}}+L_{\mathrm{e}}} \tag{21}$$

If $M_{\mathrm{E}} < M'_{\mathrm{E}}$, the failure is governed by the cross-section E-E (Fig. 23b), and the load-bearing capacity (P_{c}) can be obtained as:

$$P_{\mathrm{c}} = \frac{M_{\mathrm{E}}}{L_{\mathrm{e}}} \tag{22}$$

Otherwise, if $M_{\mathrm{E}} = M'_{\mathrm{E}}$, the failure is governed simultaneously by both cross-sections C-C and E-E (Fig. 23c), and the load-bearing capacity (P_{c}) can be obtained as:

$$P_{\mathrm{c}} = \frac{M_{\mathrm{C}}}{L_{\mathrm{c}}+L_{\mathrm{d}}+L_{\mathrm{e}}} = \frac{M_{\mathrm{E}}}{L_{\mathrm{e}}} \tag{23}$$

For the precast beam-column joint with a protruding beam, it is assumed that the moment demand of cross-section A-A (M'_{A}) is equal to its moment capacity (M_{A}). Therefore, the moment demand of the cross-sections C-C (M'_{C}) and E-E (M'_{E}) can be expressed as:

$$M'_{\mathrm{C}} = \frac{L_{\mathrm{c}}+L_{\mathrm{d}}+L_{\mathrm{e}}}{L_{\mathrm{a}}+L_{\mathrm{b}}+L_{\mathrm{c}}+L_{\mathrm{d}}+L_{\mathrm{e}}} M_{\mathrm{A}} \tag{24}$$

$$M'_{\mathrm{E}} = \frac{L_{\mathrm{e}}}{L_{\mathrm{a}}+L_{\mathrm{b}}+L_{\mathrm{c}}+L_{\mathrm{d}}+L_{\mathrm{e}}} M_{\mathrm{A}} \tag{25}$$

If $M_{\mathrm{C}} > M'_{\mathrm{C}}$ and $M_{\mathrm{E}} > M'_{\mathrm{E}}$, the failure is governed by the cross-section A-A (Fig. 23d), and the load-bearing capacity (P_{c}) can be given as:

$$P_{\mathrm{c}} = \frac{M_{\mathrm{A}}}{L_{\mathrm{a}}+L_{\mathrm{b}}+L_{\mathrm{c}}+L_{\mathrm{d}}+L_{\mathrm{e}}} \tag{26}$$

If $M_{\mathrm{C}} = M'_{\mathrm{C}}$ and $M_{\mathrm{E}} > M'_{\mathrm{E}}$, the failure is governed simultaneously by both cross-sections A-A

and C-C (Fig. 23g), and the load-bearing capacity (P_c) can be calculated as:

$$P_c = \frac{M_A}{L_a+L_b+L_c+L_d+L_e} = \frac{M_C}{L_c+L_d+L_e} \tag{27}$$

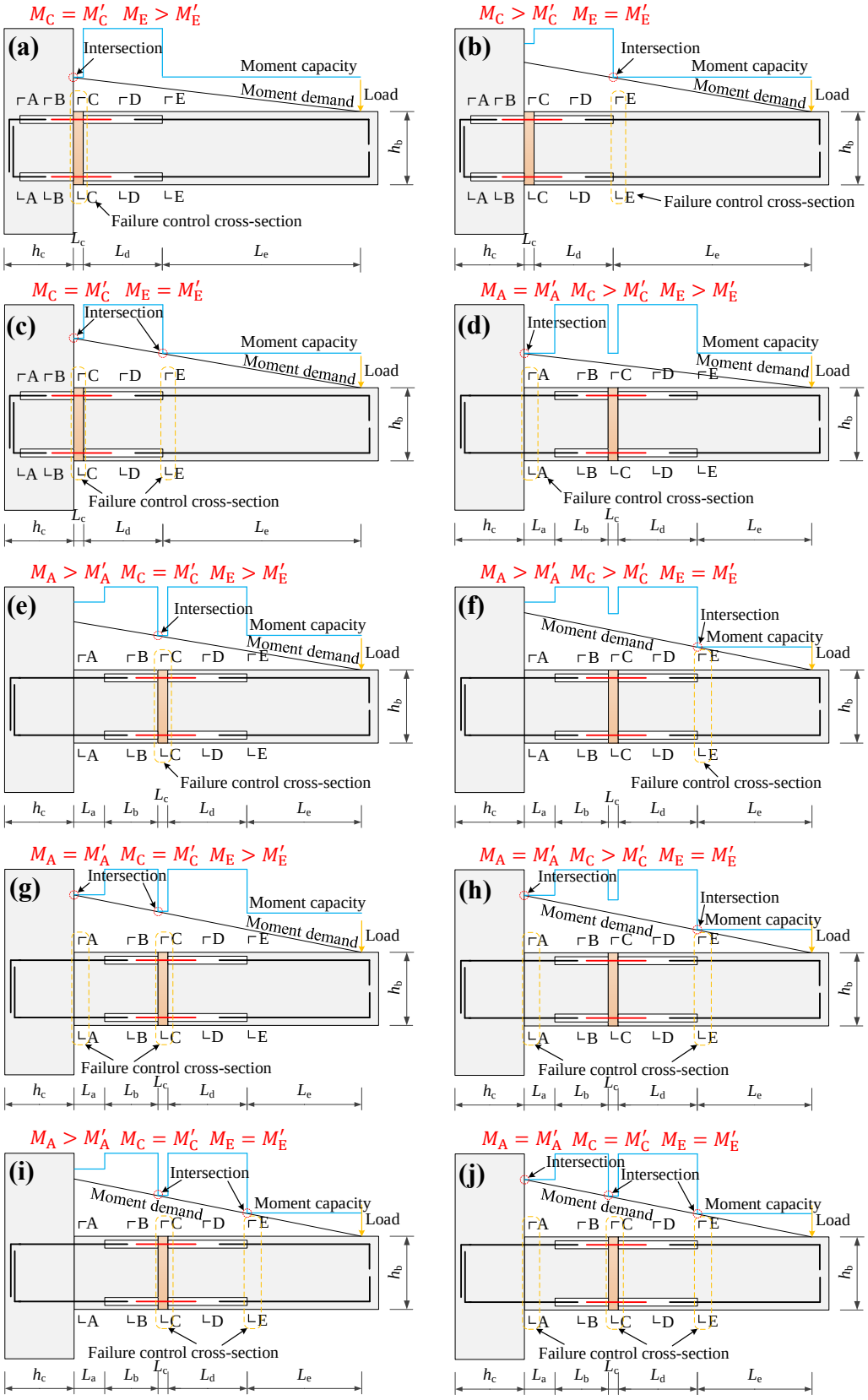

Fig. 23. Failure control cross-section of the proposed beam-column connection: (a)-(c) without a protruding beam; (d)-(j) with a protruding beam.

If $M_C > M'_C$ and $M_E = M'_E$, the failure is governed simultaneously by both cross-sections A-A and E-E (Fig. 23h), and the load-bearing capacity (P_c) can be obtained as:

$$P_c = \frac{M_A}{L_a+L_b+L_c+L_d+L_e} = \frac{M_E}{L_e} \tag{28}$$

If $M_C = M'_C$ and $M_E = M'_E$, the failure is governed simultaneously by all the cross-sections A-A, C-C, and E-E (Fig. 23j), and the load-bearing capacity (P_c) can be described as:

$$P_c = \frac{M_A}{L_a+L_b+L_c+L_d+L_e} = \frac{M_C}{L_c+L_d+L_e} = \frac{M_E}{L_e} \tag{29}$$

If $M_C < M'_C$ or $M_E < M'_E$, the cross-section A-A is not the failure control cross-section. Therefore, it is assumed that the moment demand of cross-section C-C (M'_C) is equal to its moment capacity (M_C). Thus, the moment demand of the cross-section E-E (M'_E) can be expressed as:

$$M'_E = \frac{L_e}{L_c+L_d+L_e} M_C \tag{30}$$

If $M_E > M'_E$, the failure is governed by the cross-section C-C (Fig. 23e), and the load-carrying capacity (P_c) can be obtained as:

$$P_c = \frac{M_C}{L_c+L_d+L_e} \tag{31}$$

If $M_E < M'_E$, the failure is governed by the cross-section E-E (Fig. 23f), and the load-bearing capacity (P_c) can be calculated as:

$$P_c = \frac{M_E}{L_e} \tag{32}$$

Otherwise, if $M_E = M'_E$, the failure is governed simultaneously by both cross-sections C-C and E-E (Fig. 23i), and the load-bearing capacity (P_c) can be derived as:

$$P_c = \frac{M_C}{L_c+L_d+L_e} = \frac{M_E}{L_e} \tag{33}$$

The load-carrying capacity of the proposed beam-column connection is theoretically predicted using the equations above and the existing calculation method and compared with simulation results, as listed in Table 5. P_c and P_e are the load-bearing capacities obtained using the developed approach and the existing calculation approach based on the maximum bending moment, respectively. As shown in Table 5, P_e of specimens BCJ-1-JU16-TU20 and BCJ-5-JU20-TU16 is 2.2% and 7.6% greater than the corresponding P_c, respectively, indicating that the existing calculation method can overestimate the load-bearing capacity of the proposed joint when the reinforcement ratio of different segments differs greatly; thus, the failure control cross-section should be correctly determined. In addition, the mean value and standard deviation (SD) of P_c/P_{maxn} for the joint with various

diameters of rebar are 1.01 and 0.05, respectively. Such satisfactory agreement between the calculations and simulations confirms that the load-bearing capacity of the joint connected using short and long sleeves with various reinforcement ratios in different segments can be satisfactorily predicted using the developed method.

Note that bond slip and sleeve fracture of the double-grouted sleeve splice can result in premature failure of the proposed joint. Therefore, the short and long steel sleeves used should be properly designed including sleeve length and diameter. The rebar embedded length of 8 times spliced rebar diameter is adopted to determine the lengths of the short and long sleeves because the required anchorage length of reinforcement for different types of grouted sleeves with various inner structures is experimentally found to be approximately 6-8 times spliced rebar diameter [42, 62, 66-70], and the minimum anchorage length of 8 times spliced rebar diameter is recommended in accordance with JG/T398 [71]. Thus, the requirements of the short and long sleeve lengths (L_{s}) and (L_{m}) can be expressed as below:

$$L_{\mathrm{s}} \geq 8d_{\mathrm{s}} + 8d_{\mathrm{t}} + L_{\mathrm{ad}} + 2L_{\mathrm{r}} \tag{34}$$

$$L_{\mathrm{m}} \geq 8d_{\mathrm{m}} + 16d_{\mathrm{t}} + L_{\mathrm{g}} + L_{\mathrm{ad}} + 2L_{\mathrm{r}} - L_{\mathrm{pr}} \tag{35}$$

where d_{s} and d_{m} are the embedded rebar diameters in the prefabricated ends of the short and long sleeves, respectively (Fig. 4); d_{t} is the transition rebar diameter; L_{ad} is the adjustment length added for easy installation of spliced bar considering construction tolerances and can be taken as 10-30 mm; L_{pr} is the protruding length of the transition rebar put into the long sleeve before installation, and 10 mm is recommended for it; L_{r} is the thickness of built-in sealing ring and is approximately equal to 10 mm. Note that if a rubber sleeve is used instead of the built-in sealing ring, L_{r} should be taken as zero as in this study.

According to [71], the yield and ultimate tensile bearing capacities in the middle part of both short and long sleeves (F_{gy}) and (F_{gu}) should not be lower than the maximal value of the specified yield-bearing capacity of spliced bar (F_{syk}) and 1.15 times the maximal value of the specified ultimate tensile bearing capacity of spliced bar (F_{stk}), respectively. As a result, the following equations can be obtained:

$$F_{\mathrm{gy}} = \sigma_{\mathrm{sy}} A_{\mathrm{g}} \geq F_{\mathrm{syk}} = f_{\mathrm{syk}} A_{\mathrm{s}} \tag{36}$$

$$F_{\mathrm{gu}} = \sigma_{\mathrm{sk}} A_{\mathrm{g}} \geq 1.15 F_{\mathrm{stk}} = 1.15 f_{\mathrm{stk}} A_{\mathrm{s}} \tag{37}$$

where σ_{sy} and σ_{sk} are the yield and tensile strengths of the short or long sleeve, respectively; f_{syk} and f_{stk} are the specified yield and tensile strengths of the embedded rebar in the precast part or the transition rebar, respectively; A_g is the cross-sectional area of the short or long sleeve; A_s is the cross-sectional area of the embedded rebar in the precast part or the transition rebar.

Then, the required cross-sectional area of the short or long sleeve (A_g) can be described as follows:

$$A_g \geq max\left(\frac{f_{syk}A_s}{\sigma_{sy}}, \frac{1.15f_{stk}A_s}{\sigma_{sk}}\right) \tag{38}$$

To consider construction tolerances and enable the grout to easily fill the entire space inside the sleeve, the difference (d_{diff}) between the minimal inner diameter of the sleeve and the maximal spliced rebar diameter should not be less than 10 mm [72]. Thus, the required minimal inner diameter of the short or long sleeve (D_{inner}) can be calculated as follows:

$$D_{inner} \geq max(d_{sm}, d_t) + 2t_w + d_{diff} \tag{39}$$

where d_{sm} is the diameter of the embedded rebar in the precast part; t_w is the thickness of the wedge like in this study or the height of ribs such as threaded, conical, and rectangular ribs used to prevent grout from slipping for other types of steel sleeves.

Subsequently, the required minimal outer diameter of the short or long sleeve (D_{outer}) can be obtained as

$$D_{outer} = \sqrt{\frac{4A_g}{\pi} + D_{inner}^2} \tag{40}$$

Because increasing the inner diameter of grouted sleeves can result in a decrease in confinement provided by sleeve wall on grout [62], the minimal inner diameters of the short and long sleeves determined by the approach presented above can be the recommended optimal sleeve inner diameters. Currently, there is no unified internal configuration for grouted sleeves, and different configurations can cause different efficiency of the bond between spliced rebar and grout [73]. Hence, the performance of the internal configuration designed for the short and long sleeves should be experimentally evaluated before being used for the proposed joint. As per [72], the short and long-grouted sleeve splices with grout strength of 80-95 MPa should fail by rebar fracture, or their ultimate tensile capacity should be at least 1.15 times the specified tensile capacity of spliced rebar. It should be noted that only fully-grouted couplers are considered and explored in this study. The proposed beam-column joint with other types of couplers such as half-grouted couplers is required to be further investigated.

6. Conclusions

In this study, a 3D nonlinear finite element model for a newly proposed beam-column joint connected using short and long sleeves accounting for its surface-to-surface contact behaviour between the grouting mortar and prefabricated part and strain penetration of the transition rebar is developed and validated with experimental data. A comprehensive parametric investigation is then carried out to evaluate the effects of critical factors on the structural performance of the developed joint. The main conclusions can be drawn as follows:

- The developed finite element model can well simulate the mechanical behaviour of the proposed prefabricated connection with good agreement with experimental results in terms of load-deflection response and failure modes. Stress concentration occurs in the linking region. The maximum stress of the reinforcing rebars in the joint without protruding beam is approximately 15.0% greater than that with a protruding beam length of 425 mm, indicating protruding beam can significantly affect the stress distribution of the reinforcing rebars. The maximum stress of the joint anchorage bars declines by around 87.0% when the short sleeves are placed completely in the core region of the connection. The maximal stress of all the bars in the joint with a protruding beam is close to that in the cast-in-situ counterpart.
- As the protruding beam length increases from 137.5 mm to 525 mm, the maximal crack width in the grouting mortar region drops rapidly first and then slowly with a turning point of 1.36 times the short sleeve length, and the stiffness before yielding declines as the grouted sleeves with larger stiffness are gradually far away from column face. The load-bearing capacity of the joint reaches the maximum when the protruding beam length and short sleeve length equal and thus the short sleeve length should be considered for design of protruding beam.
- With the rising grouting mortar thickness from 30 mm to 110 mm, the maximum stress of the tension transition rebar declines rapidly first and then slowly with an inflexion point of a grouting mortar thickness of 50 mm, but the damage of the grouting mortar gradually increases as the improved deformation capacity of the tension transition rebar resulting from its increased length reduces the stress concentration of rebar.
- For the joint with no protruding beam, as the tension linking bar diameter increases from 16 mm to 20 mm, the yield and ultimate load-bearing capacity is enhanced by 55.5% and 37.8%, respectively, while the maximum crack width in the linking region drops by 72.6% with a damage

location at the end of the long-grouted coupler near the side of loading point. These indicate that the tension capacity of the transition rebar can significantly affect the load-carrying ability and failure mode of the joint without a protruding beam.

- For the joint with a projecting beam, increasing the diameter of the tension joint anchorage bar obviously increases the load-bearing capacity and stiffness as well as the crack width in the grouting mortar zone. However, a continuous rise in the diameter of the tension joint anchorage rebar cannot continuously improve the yield load unless the tension linking bar diameter increases simultaneously. The damage locations of the joint with a protruding beam cannot be completely controlled by only altering the joint anchorage rebar diameter.
- The eccentricity of the tension transition rebar has almost no impact on the load-carrying capacity of the connection with a projecting beam. The protruding beam can help reduce the negative impact of eccentricity of the transition rebar. The increment of the maximal crack width for the joint with a protruding beam is 69.2% lower than that with no protruding beam.

Acknowledgments

The authors gratefully acknowledge the financial support from the Hainan Province Science and Technology Special Fund (Grant No. ZDKJ2021024) and the Scientific and Technological Plan Project of Wuhan Urban and Rural Construction Bureau (Grant No. 202023). The financial support provided by China Scholarship Council (CSC) to the first author is also gratefully acknowledged.

References

[1] Xue W, Hu X, Dai L, Zhu B. Cyclic behavior of semi-rigid precast concrete beam-to-column subassemblages with rapid assembly connections. Journal of Building Engineering 2022;46:103671.

[2] Ameli MJ, Pantelides CP. Seismic analysis of precast concrete bridge columns connected with grouted splice sleeve connectors. Journal of Structural Engineering 2016;143(2):04016176.1-04016176.13.

[3] Guan D, Guo Z, Xiao Q, Zheng Y. Experimental study of a new beam-to-column connection for precast concrete frames under reversal cyclic loading. Advances in Structural Engineering 2016;19(3):529-545.

[4] Elsanadedy HM, Al-Salloum YA, Alrubaidi MA, Almusallam TH, Abbas H. Finite element analysis for progressive collapse potential of precast concrete beam-to-column connections

strengthened with steel plates. Journal of Building Engineering 2021;34:101875.

[5] Yang J, Guo T, Chai S. Experimental and numerical investigation on seismic behaviours of beam-column joints of precast prestressed concrete frame under given corrosion levels. Structures 2020;27:1209-1221.

[6] Department of Housing and Urban-Rural Development of Jiangxi Province. Some opinions on accelerating the development of prefabricated buildings. <http://www.jiangxi.gov.cn/art/2020/12/21/art_14325_3003202.html?xxgkhide=1>. December 21, 2020.

[7] Jiangsu Provincial People's Government. Opinions of the Jiangsu Provincial Government on accelerating the modernization of the construction industry and promoting the transformation and upgrading of the construction industry. <http://www.jiangsu.gov.cn/art/2014/12/9/art_46666_2569593.html>. October 31, 2014.

[8] General Office of the People's Government of Beijing Municipality. Implementation opinions of the General Office of the People's Government of Beijing Municipality on further developing fabricated buildings. <http://www.beijing.gov.cn/zhengce/zfwj/zfwj2016/bgtwj/202204/t20220429_2698683.html>. April 25, 2022.

[9] Hu G, Huang W, Xie H. Mechanical behavior of a replaceable energy dissipation device for precast concrete beam-column connections. Journal of Constructional Steel Research 2020;164:105816.

[10] Batalha N, Rodrigues H, Arêde A, Furtado A, Sousa R, Varum H. Cyclic behaviour of precast beam-to-column connections with low seismic detailing. Earthquake Engineering & Structural Dynamics 2022;51(5):1096-1114.

[11] Kurama YC, Sritharan S, Fleischman RB, Restrepo JL, Henry RS, Cleland NM, Ghosh SK, Bonelli P. Seismic-resistant precast concrete structures: State of the art. Journal of Structural Engineering 2018;144:031180014.

[12] Liu H, Wang Z, Du X, Shen GQ. The seismic behaviour of precast concrete interior joints with different connection methods in assembled monolithic subway station. Engineering Structures 2021;232:111799.

[13] Ruggieri S, Vukobratović V. Acceleration demands in single-storey RC buildings with flexible

diaphragms. Engineering Structures 2023;275:115276.

[14] Ruggieri S, Porco F, Uva G. A practical approach for estimating the floor deformability in existing RC buildings: evaluation of the effects in the structural response and seismic fragility. Bulletin of earthquake engineering 2020;18(5):2083-2113.

[15] Lacerda MMS, da Silva TJ, Alva GMS, de Lima MCV. Influence of the vertical grouting in the interface between corbel and beam in beam-to-column connections of precast concrete structures - An experimental analysis. Engineering Structures 2018;172:201-213.

[16] Clementi F, Scalbi A, Lenci S. Seismic performance of precast reinforced concrete buildings with dowel pin connections. Journal of Building Engineering 2016;7:224-238.

[17] Zoubek B, Fischinger M, Isakovic T. Estimation of the cyclic capacity of beam-to-column dowel connections in precast industrial buildings. Bulletin of Earthquake Engineering 2015;13(7):2145-2168.

[18] Brunesi E, Nascimbene R, Bolognini D, Bellotti D. Experimental investigation of the cyclic response of reinforced precast concrete framed structures. PCI Journal 2015;60(2):57-79.

[19] Ding T, Xiao J, Chen E, Khan A. Experimental study of the seismic performance of concrete beam-column frame joints with DfD connections. Journal of Structural Engineering 2020;146(4):04020036.

[20] Korkmaza HH, Tankut T. Performance of a precast concrete beam-to-beam connection subject to reversed cyclic loading. Engineering Structures 2005;27(9):1392-1407.

[21] Xiao J, Ding T, Zhang Q. Structural behavior of a new moment-resisting DfD concrete connection. Engineering Structures 2017;132:1-13.

[22] Ersoy U, Tankut T. Precast concrete members with welded plate connections under reversed cyclic loading. PCI Journal 1993;38(4):94-100.

[23] Guerrero H, Rodriguez V, Escobar JA, Alcocer SM, Bennetts F, Suarez M. Experimental tests of precast reinforced concrete beam-column connections. Soil Dynamics and Earthquake Engineering 2019;125:105743.

[24] Huang W, Hu G, Zhang J. Experimental study on the seismic performance of new precast concrete beam-column joints with replaceable connection. Structures 2022;35:856-872.

[25] Nzabonimpa JD, Hong WK, Kim J. Experimental and non-linear numerical investigation of the novel detachable mechanical joints with laminated plates for composite precast beam-column

joint. Composite Structures 2018;185:286-303.

[26] Bahrami S, Madhkhan M, Shirmohammadi F, Nazemi N. Behavior of two new moment resisting precast beam-column connections subjected to lateral loading. Engineering Structures 2017;132:808-821.

[27] Yang C, Li A, Xie L. Development of design method for precast concrete frame with dry-connected rotational friction dissipative beam-to-column joints. Journal of Building Engineering 2022;45:103563.

[28] Yuan Y, Huang H, Ye Y, Li M, Sun H. Performance coordination design method applied to replaceable artificial controllable plastic hinge for precast concrete beam-column joints. Journal of Building Engineering 2022;47:103863.

[29] Li Z, Qi Y, Teng J. Experimental investigation of prefabricated beam-to-column steel joints for precast concrete structures under cyclic loading. Engineering Structures 2020;209:110217.

[30] Rodgers GW, Solberg KM, Mander JB, Chase JG, Bradley BA, Dhakal RP. High-force-to-volume seismic dissipators embedded in a jointed precast concrete frame. Journal of Structural Engineering 2012;138(3):375-386.

[31] Wang CL, Liu Y, Zheng X, Wu J. Experimental investigation of a precast concrete connection with all-steel bamboo-shaped energy dissipaters. Engineering Structures 2019;178:298-308.

[32] Priestley MJN, Tao JR. Seismic response of precast prestressed concrete frames with partially debonded tendons. PCI Journal 1993;38(1):58-69.

[33] Guo T, Song L, Yang K, Zhu R, Tesfamariam S. Experimental investigation and numerical simulation of self-centering concrete frames with sliding infill walls. Journal of Building Engineering 2022;52:104435.

[34] Wang H, Marino EM, Pan P, Liu H, Nie X. Experimental study of a novel precast prestressed reinforced concrete beam-to-column joint. Engineering Structures 2018;156:68-81.

[35] Huang L, Zhou Z, Huang X, Wang Y. Variable friction damped self-centering precast concrete beam–column connections with hidden corbels: Experimental investigation and theoretical analysis. Engineering Structures 2020;206:110150.

[36] Yu J, Zhang W, Tang Z, Guo X, Pospíšil S. Seismic behavior of precast concrete beam-column joints with steel strand inserts under cyclic loading. Engineering Structures 2020;216:110766.

[37] Fan JJ, Wu G, Feng DC, Zeng YH, Lu Y. Seismic performance of a novel self-sustaining beam-

column connection for precast concrete moment-resisting frames. Engineering Structures 2020;222:111096.

[38] Zhang ZY, Ding R, Nie X, Fan JS. Seismic performance of a novel interior precast concrete beam-column joint using ultra-high performance concrete. Engineering Structures 2020;222:111145.

[39] Parastesh H, Hajirasouliha I, Ramezani R. A new ductile moment-resisting connection for precast concrete frames in seismic regions: An experimental investigation. Engineering Structures 2014;70:144-157.

[40] Liu Y, Cai J, Deng X, Cao Y, Feng J. Experimental study on effect of length of service hole on seismic behavior of exterior precast beam-column connections. Structural Concrete 2019;20(1):85-96.

[41] Yan Q, Chen T, Xie Z. Seismic experimental study on a precast concrete beam-column connection with grout sleeves. Engineering Structures 2018;155:330-344.

[42] Lu Z, Huang J, Li Y, Dai S, Peng Z, Liu X, Zhang M. Mechanical behaviour of grouted sleeve splice under uniaxial tensile loading. Engineering Structures 2019;186:421-435.

[43] Dabiri H, Kheyroddin A, Dall'Asta A. Splice methods used for reinforcement steel bars: A state-of-the-art review. Construction and Building Materials 2022;320:126198.

[44] Feng B, Xiong F, Chen J, Chen W, Zhang Y. Effects of postcast connection locations on the seismic performance of precast concrete frame joints. The Structural Design of Tall and Special Buildings 2018;27(18):e1544.

[45] Ma C, Jiang H, Wang Z. Experimental investigation of precast RC interior beam-column-slab joints with grouted spiral-confined lap connection. Engineering Structures 2019;196:109317.

[46] Henin E, Morcous G. Non-proprietary bar splice sleeve for precast concrete construction. Engineering Structures 2015;83:154-162.

[47] Koshikawa T. Moment and energy dissipation capacities of post-tensioned precast concrete connections employing a friction device. Engineering Structures 2017;138:170-180.

[48] Lu Z, Huang J, Dai S, Liu J, Zhang M. Experimental study on a precast beam-column joint with double grouted splice sleeves. Engineering Structures 2019;199:109589.

[49] Feng DC, Wu G, Lu Y. Finite element modelling approach for precast reinforced concrete beam-to-column connections under cyclic loading. Engineering Structures 2018;174:49-66.

[50] Wan S, Loh CH, Peng SY. Experimental and theoretical study on softening and pinching effects of bridge column. Soil Dynamics and Earthquake Engineering 2001;21(1):75-81.

[51] Ali A, Kim D, Cho SG. Modeling of nonlinear cyclic load behavior of I-shaped composite steel-concrete shear walls of nuclear power plants. Nuclear Engineering and Technology 2013;45(1):89-98.

[52] Peng Z, Dai S, Pi YL, Zhang Y, Huang J. Seismic performance of end-plate connections between T-shaped CFST columns and RC beams. Journal of Constructional Steel Research 2018;145:167-183.

[53] Nzabonimpa JD, Hong WK. Experimental and nonlinear numerical analysis of precast concrete column splices with high-yield metal plates. Journal of Structural Engineering 2019;145(2):040182542.

[54] Nzabonimpa JD, Hong WK. Structural performance of detachable precast composite column joints with mechanical metal plates. Engineering Structures 2018;160:366-382.

[55] Han Q, Sakata H, Maida Y, Mori T, Maegawa T, Zhang Y. Performance evaluation of RC frame with RC wall piers equipped with unbonded steel rod dampers subjected to in-plane loading. Engineering Structures 2019;197:109403.

[56] Pathirana, SW, Uy B, Mirza O, Zhu X. Flexural behaviour of composite steel-concrete beams utilising blind bolt shear connectors. Engineering Structures 2016;114:181-194.

[57] Jumaa GB, Yousif AR. Numerical modeling of size effect in shear strength of FRP-reinforced concrete beams. Structures 2019;20:237-254.

[58] GB50010-2010. Code for design of concrete structures. Beijing: China Architecture and Building Press; 2010.

[59] EN 1992-1-1: 2004. Brussels: Eurocode 2: Design of concrete structures; 2004.

[60] Hu X, Xue W, Zhang B. Cyclic response of concrete frame with precast column and U-shaped composite beam, Structures. 43 (2022) 465-478.

[61] Chen J, Wang Z, Liu Z, Ju S. Experimental investigation of mechanical behaviour of rebar in steel half-grouted sleeve connections with defects in water/binder ratio. Structures 2020;26:487-500.

[62] Ling JH, Abd. Rahman AB, Ibrahim IS, Hamid ZA. Tensile capacity of grouted splice sleeves. Engineering Structures 2016;111:285-296.

[63] Einea A, Yamane T, Tadros MK. Grout-filled pipe splices for precast concrete construction. PCI Journal 1995;40(1):82-93.

[64] Wang Z, Zhu J, Wang J, Zhao G, Sun S, Zhang J. UHPC grout-filled pipe sleeve with bolts for large-diameter deformed bars: Analytical model on the tensile resistance and design method. Engineering Structures 2021;245:112851.

[65] Xu T, Li Q, Zhao R, Ding J, Zhan Y. On the early-age bond-slip behavior of an eccentric bar embedded in a grouted sleeve. Engineering Structures 2019;190:160-170.

[66] Wang L, Song Y, Han Q, Wang Z. Experimental investigation on the dynamic behavior of grouted splice sleeve connector under fast tensile loading. Journal of Building Engineering 2023;66:105927.

[67] Li Y, Zhang L, Zhang Q, He X, Wang J, Su Y. Anchorage behavior of grouting sleeves under uniaxial and cyclic loading-A comparative study of the internal structure of sleeves. Journal of Building Engineering 2022;49:104057.

[68] Ghayeb HH, Razak HA, Sulong NR, Mo KH, Abutaha F, Gordan M. Performance of mechanical steel bar splices using grouted couplers under uniaxial tension. Journal of Building Engineering 2021;34:101892.

[69] Liu C, Pan L, Liu H, Tong H, Yang Y, Chen W. Experimental and numerical investigation on mechanical properties of grouted-sleeve splices. Construction and Building Materials 2020;260:120441.

[70] Zheng Y, Guo Z, Guan D, Zhang X. Parametric study on a novel grouted rolling pipe splice for precast concrete construction. Construction and Building Materials 2018;166:452-463.

[71] JG/T398-2019. The grouting sleeve for rebars splicing. Beijing: Standards Press of China; 2019.

[72] JGJ355-2015. Technical specification for grout sleeve splicing for rebars. Beijing: China Architecture and Building Press; 2015.

[73] Ling JH, Abd. Rahman AB, Ibrahim IS. Feasibility study of grouted splice connector under tensile load. Construction and Building Materials 2014;50(1):530-539.